Check for updates

Tectonics®

RESEARCH ARTICLE
10.1029/2023TC007765

Michaël Pons and Constanza Rodriguez Piceda contributed equally to this work.

Key Points:

- A data-driven modeling workflow is applied to the southern Central Andes to assess the contribution of the subducting and overriding plates on strain localization in the overriding plate
- The subducting flat slab cools and strengthens the continental lithosphere above it. Stresses related to the interaction between the oceanic Nazca Plate and the continental South American Plate is transmitted toward the eastern Sierras Pampeanas in the broken foreland of the orogen
- Inherited faults amplify surface strain localization in the foreland. High topography inhibits strain localization in the orogen. Consequently, strain migrates toward the Andean foreland

Supporting Information:

Supporting Information may be found in the online version of this article.

Correspondence to:

M. Pons,
ponsm@gfz-potsdam.com

Citation:

Pons, M., Rodriguez Piceda, C., Sobolev, S. V., Scheck-Wenderoth, M., & Strecker, M. R. (2023). Localization of deformation in a non-collisional subduction orogen: The roles of dip geometry and plate strength on the evolution of the broken Andean foreland, Sierras Pampeanas, Argentina. *Tectonics*, *42*, e2023TC007765. https://doi.org/10.1029/2023TC007765

Received 20 JAN 2023
Accepted 19 JUL 2023

© Wiley Periodicals LLC. The Authors. This is an open access article under the terms of the Creative Commons Attribution License, which permits use, distribution and reproduction in any medium, provided the original work is properly cited.

Localization of Deformation in a Non-Collisional Subduction Orogen: The Roles of Dip Geometry and Plate Strength on the Evolution of the Broken Andean Foreland, Sierras Pampeanas, Argentina

Michaël Pons[1,2], Constanza Rodriguez Piceda[1,2,3], Stephan V. Sobolev[1,2], Magdalena Scheck-Wenderoth[2,4], and Manfred R. Strecker[1]

[1]Universität Potsdam, Institut für Geowissenschaften, Potsdam, Germany, [2]Helmholtz-Zentrum Potsdam GFZ - Deutsches GeoForschungsZentrum, Potsdam, Germany, [3]School of Geography Earth and Environmental Sciences, Plymouth University, Plymouth, UK, [4]RWTH Aachen University, Aachen, Germany

Abstract The southern Central Andes (SCA, 27°–40°S) exhibit a complex deformation pattern that is influenced by multiple factors, including the present-day dip angle of the subducting oceanic Nazca plate and the influence of inherited heterogeneities in the continental South American plate. This study employs a data-driven geodynamic workflow to assess the role of various forcing factors in determining upper-plate strain localization, both above the flat slab and the steeper segment to the south. These include the dip angle of the Nazca plate, the mechanically weak sedimentary basins, the thickness and composition of the continental crust, the strength of the subduction interface, and the plate velocities. Our modeling results predict two main deformation modes: (a) pure-shear shortening in the broken foreland above the flat-slab segment and eastward propagation of deformation, and (b) simple-shear shortening restricted to the eastern margin of the Andean fold-and-thrust belt above the steep-slab segment. While the convergence velocity and the frictional strength of the subduction interface primarily control the intensity of the deformation, inherited heterogeneities tend to localize deformation, and weak sediments leads to intensified surface deformation. Thicker crust and surface topography also influences strain localization by transferring stress to the eastern orogenic front. Above the flat-slab segment deformation migrates eastward, which is facilitated by enhanced interface coupling. The transition between the steep and sub-horizontal subduction segments is characterized by a diffuse transpressional shear zone, likely controlled by the change in dip geometry of the Nazca plate, and the presence of inherited faults and weak sedimentary basins.

Plain Language Summary The deformation patterns in the southern part of the Central Andes, where the oceanic Nazca plate subducts beneath the continental South American Plate, exhibit great variability both along and across the mountain range and the adjacent regions. However, the extent to which each plate contributes to these patterns remains a topic of ongoing discussion. In this study, we use a computer code to numerically simulate the forces that act on specified areas of the mountain belt (stresses) and resulting deformation (strain), by incorporating the present-day plate geometry, temperature, and composition into our workflow. This enables us to quantify the relative contribution of each plate to observable deformation patterns, including variations in the dip angle of the oceanic plate and the influence of mechanically weak discontinuities within the continental plate that were inherited from previous tectonic processes.

1. Introduction

The central part of the Cenozoic Andes, located at the convergent margin where the oceanic Nazca plate subducts beneath the continental South American Plate, provide a natural laboratory to study strain localization processes in a non-collisional mountain belt and its neighboring regions (Burchfiel, 1980). Spanning a length of 6,000 km, this mountain range exhibits varying characteristics, including segments with and without arc magmatism and the development of fold-and-thrust belts (FTBs) with different structural styles and degrees of shortening (Jordan et al., 1983a; Jordan et al., 1983b). In the southern Central Andes (SCA, 27°–40°S), the mechanisms responsible for the observed variability in the foreland deformation patterns have been the subject of debate, with two proposed end-member models. The first one is related to the effect of the subduction of a subhorizontal oceanic plate between 27° and 33°S in a segment known as the Pampean flat slab (Figure 1a, Barazangi & Isacks, 1976, 1979;

Author Contributions:
Conceptualization: Michaël Pons, Constanza Rodriguez Piceda
Data curation: Michaël Pons, Constanza Rodriguez Piceda
Formal analysis: Michaël Pons, Constanza Rodriguez Piceda
Funding acquisition: Manfred R. Strecker
Investigation: Michaël Pons, Constanza Rodriguez Piceda
Methodology: Michaël Pons, Constanza Rodriguez Piceda, Stephan V. Sobolev, Magdalena Scheck-Wenderoth, Manfred R. Strecker
Project Administration: Manfred R. Strecker
Software: Michaël Pons, Constanza Rodriguez Piceda
Supervision: Stephan V. Sobolev, Magdalena Scheck-Wenderoth, Manfred R. Strecker
Validation: Stephan V. Sobolev, Magdalena Scheck-Wenderoth, Manfred R. Strecker
Visualization: Michaël Pons, Constanza Rodriguez Piceda
Writing – original draft: Michaël Pons, Constanza Rodriguez Piceda
Writing – review & editing: Michaël Pons, Constanza Rodriguez Piceda, Stephan V. Sobolev, Magdalena Scheck-Wenderoth, Manfred R. Strecker

Ramos & Scientific, 2002). In this model, the flattening of the slab produces a bulldozing effect oriented to the keel of the continental lithosphere, where shear stresses are transmitted from the subduction zone interface at the trench to the eastern edge of the flat-slab segment (e.g., Gutscher, 2018; Horton, 2018; Jordan et al., 1984; Martinod et al., 2010; Ramos & Folguera, 2009). The second mechanism involves compressional reactivation of pre-existing crustal faults inherited from previous tectonic regimes that act as zones of weakness, promoting strain localization (Cristallini & Ramos, 2000; Giambiagi et al., 2014; Kley & Monaldi, 1998; Lossada et al., 2017; Mescua et al., 2014; Mon & Salfity, 1995), similar to the inverted Cretaceous extensional province of the Santa Bárbara System of Argentina farther north (Mon & Salfity, 1995). Other factors contributing to strain localization in the upper-plate are crustal-scale heterogeneities in this plate, including compositional and thickness variations (Barrionuevo et al., 2021; Gerbault et al., 2009; Giambiagi et al., 2022; Liu et al., 2022; Rodriguez Piceda, Scheck-Wenderoth, Bott, et al., 2022; Rodriguez Piceda, Scheck-Wenderoth, Cacace, et al., 2022). Assessing the relative contribution of these various factors to strain localization in the SCA is crucial to better understand plate interaction and deformation processes at non-collisional convergent plate margins.

Flat subduction is a geodynamic process that occurs at approximately 10% of active convergent margins (Gutscher et al., 2000). In the SCA, supporting evidence for the existence of the Pampean flat slab includes the sub-horizontal distribution of seismicity far away from the plate margin (Barazangi & Isacks, 1976, 1979) and a gap in volcanic activity that has existed since the late Miocene (Isacks & Barazangi, 1977; Jordan, Isacks, Ramos, & Allmendinger, 1983; Jordan, Isacks, & Ramos, 1983). It has been proposed that slab flattening may be caused by the subduction of buoyant ridges or oceanic plateaus (Espurt et al., 2008; Gutscher et al., 2000), but more recent thermo-mechanical modeling work suggests that the present-day thickness of the oceanic crust is not sufficient to sustain this dip geometry over long distances (Schellart, 2020; Schellart & Strak, 2021). Other authors have proposed that a short slab (~300 km length) may potentially be related to slab break-off (Gao et al., 2021), resulting in a decrease of the slab-pull force, late-stage eclogitization of oceanic crust, and ultimately flat subduction (Dai et al., 2020; Gerya et al., 2009; Liu & Currie, 2016; Van Hunen et al., 2002). Alternatively, the westward drift of the continental plate (Schellart & Strak, 2021) may have facilitated hydration of the mantle wedge (Manea & Gurnis, 2007) and would have caused a suction effect of the mantle wedge, thereby promoting the flattening of the slab.

In the SCA, the Pampean flat slab is associated with the subduction of the Juan-Fernandez Ridge (JFR) bathymetric high (Figure 1; Bello-González et al., 2018; Gutscher et al., 2000; Kley, 1999; Yáñez et al., 2001). Due to the oblique subduction and reconstructed shape of the ridge, the Pampean flat slab is thought to have migrated from ~20°S to its present-day position at ~32°S within the last 35 Ma (Yáñez et al., 2001). The tectono-magmatic evolution of the orogen was significantly influenced by this process, as evidenced by the increase of shortening magnitude following the migration of the flat slab (Dickinson & Snyder, 1978; Haines et al., 2001; Jordan & Allmendinger, 1986; Jordan, Isacks, Ramos, & Allmendinger, 1983; Jordan, Isacks, & Ramos, 1983; Kay & Mpodozis, 2002; Oncken et al., 2006, 2012; Pilger, 1981; Ramos & Scientific, 2002).

The deformation style in the SCA foreland exhibits significant variability along strike. Above the flat slab segment, the Precordillera fold-and-thrust belt along the eastern flank of the orogen displays mixed deformation characteristics with thin-skinned deformation over a westward-dipping décollement (Allmendinger & Judge, 2014; Zapata & Allmendinger, 1996) and crustal thickening in basement sectors below (Figure 1b, Gans et al., 2011; Giambiagi et al., 2011; Zapata & Allmendinger, 1996). East of the Precordillera follows the thick-skinned broken foreland of the reverse-faulted Sierras Pampeanas morphotectonic province between 27° and 33°S (Figure 1b, Jordan, Isacks, Ramos, & Allmendinger, 1983; Jordan, Isacks, & Ramos, 1983; Ramos & Scientific, 2002). Via a region between 33° and 36°S where both thick-skinned and thin-skinned deformation styles coexist the foreland transitions into predominant thin-skinned deformation south of ~36°S (Figures 1c and 1d, Fuentes et al., 2016; Giambiagi et al., 2012; Jordan & Allmendinger, 1986; Manceda & Figueroa, 1995) while the basement remains mostly undeformed (Figure 1d). In this transition, the San Rafael region exhibits thick-skinned deformation (Heredia et al., 2016), whereas the Cerrilladas Pedemontanas region displays thin-skinned deformation (Figure 1c, Ahumada & Costa, 2009).

In this study, we aim at quantifying the relative importance of the key contributors to strain localization in the upper plate of the SCA and their influence on different foreland deformation styles. We used data-driven geodynamic modeling to simulate rapid strain localization within the lithosphere of the SCA, incorporating the current 3D structural, density, and thermal configuration of the oceanic and continental plates (Rodriguez Piceda et al., 2021; Rodriguez Piceda, Scheck-Wenderoth, Bott, et al., 2022). In our analysis, we distinguish between shallow and deep-seated contributors that affect the deformation of the crust or the entire lithosphere, respectively. At the surface,

19449194, 2023, 8, Downloaded from https://agupubs.onlinelibrary.wiley.com/doi/10.1029/2023TC007765 by Rwth Aachen Hochschulbibliothe, Wiley Online Library on [15/01/2024]. See the Terms and Conditions (https://onlinelibrary.wiley.com/terms-and-conditions) on Wiley Online Library for rules of use; OA articles are governed by the applicable Creative Commons License

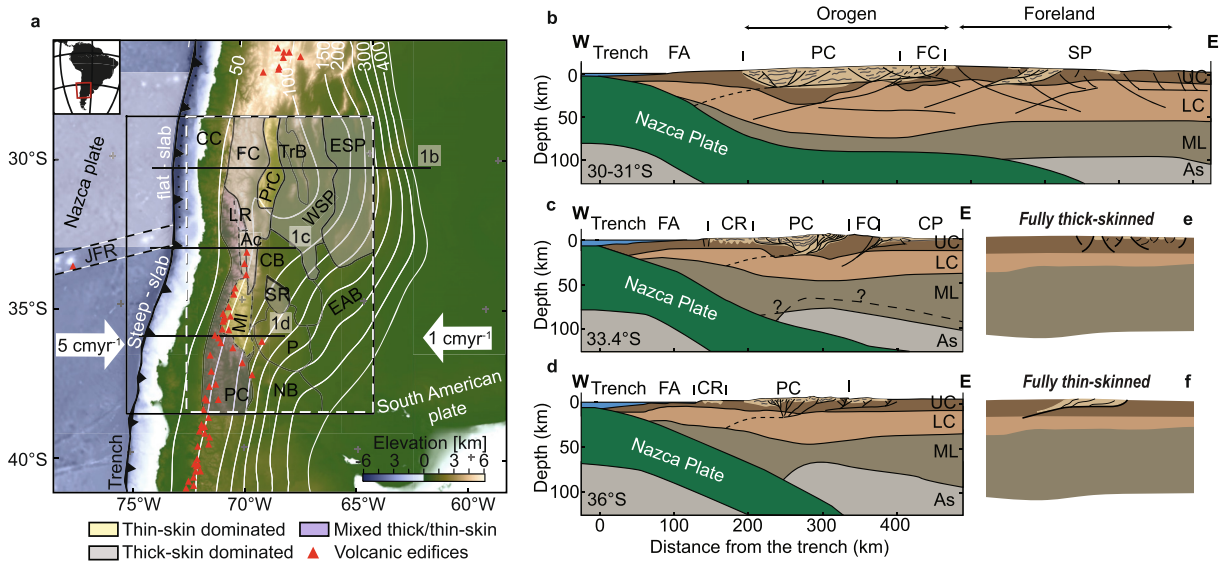


Figure 1. Structural cross sections and map of the Southern Central Andes. (a) topography and bathymetry of the model area based on ETOPO1 global relief model (Amante & Eakins, 2009), indicating the modeling area with greater resolution (black rectangle) and the borders of the morphotectonic provinces (modified from Rodriguez Piceda et al., 2021) color-coded by the dominant style of deformation. The white-dashed rectangle outlines the extent of the gravity-constrained structural model (Rodriguez Piceda et al., 2021). Red triangles depict volcanic edifices with Holocene to Quaternary volcanic activity (Global GIS: volcanoes of the world; volcano basic data, 2003). Depth contours of the top slab from Slab2 (Hayes et al., 2018) are shown in white lines. Dashed black lines in the oceanic domain delimit the Juan Fernandez Ridge (JFR). Oceanic and continental plate velocities are indicated by white arrows (Becker et al., 2015; Sdrolias & Müller, 2006). Abbreviations of main morphotectonic provinces: CB: Cuyo basin, CC: Coastal Cordillera, CP: Cerrilladas Pedemontanas, ESP: Eastern Sierras Pampeanas, NB: Neuquén basin; P: Payenia, PC: Principal Cordillera (LR: La Ramada fold-thrust belt, Ac: Aconcagua fold-thrust belt, Ml: Malargüe fold-thust belt), FC: Frontal Cordillera, FA: forearc, PrC: Precordillera, SR: San Rafael Block, TrB: Triassic basins, WSP: Western Sierras Pampeanas, EAB: Extra-Andean basins. (b) Transect between 30 and 31°S (modified from Gans et al., 2011; Lossada et al., 2017; Ramos & Scientific, 2002; Stalder et al., 2020) (c) Transect at 33.4°S (modified from Barrionuevo et al., 2021). (d) Transect at 36°S (modified from Barrionuevo et al., 2021). Abbreviations of lithospheric and asthenospheric units: UC: upper crust, LC: lower crust, ML: mantle lithosphere, Ast: asthenosphere. Light-brown colored area indicates crustal regions with pronounced deformation. (e) schematic diagram of thick-skinned deformation. (f) schematic diagram of thin-skinned deformation.

we consider the effect of topography, and the strength and spatial distribution of mechanically weak sedimentary rocks. The latter factor is primarily a function of the existence of individual sedimentary basins that developed during Mesozoic extensional processes (Barredo & Sharkov, 2012; Franzese et al., 2003; Uliana et al., 1989); the normal faults that once bounded these sedimentary basins were subsequently reactivated during Cenozoic Andean compression (Fennell et al., 2019; Mpodozis & Kay, 1990; Uliana et al., 1995). Low frictional strength of unconsolidated sediments or poorly lithified sedimentary rocks may favor strain localization and thin-skinned deformation (Allmendinger et al., 1997; Allmendinger & Gubbels, 1996; Babeyko & Sobolev, 2005; Kley, 1999; Liu et al., 2022). Therefore, by including sedimentary basins in our model, we examined the role of crustal-scale heterogeneities. At greater depths, strain localization can be affected by lithospheric-scale heterogeneities, such as discrete suture zones that developed during the amalgamation of Paleozoic terranes (e.g., Ramos, 2010). Other crustal-scale heterogeneities are volumetric discontinuities associated with inherited variations in the composition and/or thickness of the layers of the continental lithosphere (i.e., crystalline crust and lithospheric mantle), which reflect the tectono-magmatic evolution of different sectors within the orogen and its foreland (Ibarra et al., 2018, 2019; Liu et al., 2022; Rodriguez Piceda et al., 2021; Tassara & Echaurren, 2012; Tassara et al., 2006). Combined, these structural and geometric parameters may influence lithospheric strength and the localization of deformation (Barrionuevo et al., 2021; Giambiagi et al., 2012; Horton et al., 2016, 2022; Lossada et al., 2017; Marot et al., 2014; Ramos & Folguera, 2009; Ramos & Scientific, 2002). Ultimately, our analysis sheds new light on the long-standing debate concerning the role and degree of influence of flat-slab geometry and inherited crustal-scale heterogeneities on deformation styles in orogenic forelands.

2. Methods

2.1. Governing Equations

We used the finite-element code ASPECT (Advanced Solver for Problems in Earth's ConvecTion, version 2.3.0-pre, Bangerth et al., 2021; Heister et al., 2017; Kronbichler et al., 2012; Rose et al., 2017) to simulate brittle and

19449194, 2023, 8, Downloaded from https://agupubs.onlinelibrary.wiley.com/doi/10.1029/2023TC007765 by Rwth Aachen Hochschulbibliothe, Wiley Online Library on [15/01/2024]. See the Terms and Conditions (https://onlinelibrary.wiley.com/terms-and-conditions) on Wiley Online Library for rules of use; OA articles are governed by the applicable Creative Commons License

19449194, 2023, 8, Downloaded from https://agupubs.onlinelibrary.wiley.com/doi/10.1029/2023TC007765 by Rwth Aachen Hochschulbibliothe, Wiley Online Library on [15/01/2024]. See the Terms and Conditions (https://onlinelibrary.wiley.com/terms-and-conditions) on Wiley Online Library for rules of use; OA articles are governed by the applicable Creative Commons License

ductile deformation. This code solves for conservation of the momentum (Equation 1), mass (Equation 2) and energy (Equation 3). In addition, the advection and reaction equation depicts the transportation of compositional fields along the velocity field (Equation 4):

$$\nabla \cdot \boldsymbol{u} = 0, \tag{1}$$

$$-\nabla \cdot (2\eta\dot{\varepsilon}) + \nabla P = \rho g, \tag{2}$$

$$\varrho C p \left(\frac{\partial T}{\partial t} + \boldsymbol{u} \cdot \nabla T\right) - \nabla \cdot k\nabla T = (2\eta\dot{\varepsilon}) : \dot{\varepsilon} - \alpha T \boldsymbol{u} \cdot g, \tag{3}$$

$$\frac{\partial c_i}{\partial t} + \boldsymbol{u} \cdot \nabla c_i = q_i, \tag{4}$$

Where $\dot{\varepsilon} = \frac{1}{2} \cdot (\nabla \boldsymbol{u} + (\nabla \boldsymbol{u})^T$, is the deviatoric strain rate tensor; $\boldsymbol{u} = u(\vec{x}, t)$, $P = p(\vec{x}, t)$ and $T = T(\vec{x}, t)$ are the velocity, pressure and thermal fields, respectively. g is the acceleration of gravity, C_p is the heat capacity, ρ is the density, ϱ is the reference density (see Equation 5), k is the thermal conductivity, α is the thermal expansivity, η is the viscosity, t is time, c_i is the composition, and q_i is the reaction rate. The energy equation (Equation 3) includes shear heating and adiabatic heating, while the contribution of radiogenic heating to the temperatures is already included in the initial thermal condition.

To simulate realistic densities, we used the equation of state of Murnaghan (1944, Equation 5) which takes into account pressure, although the latter is neglected in the mass-conservation conversion equation (Equation 2). This assumption can be considered as an acceptable approximation since in subduction models compressibility is considered to have a negligible effect on the subduction dynamics (Fraters, 2015).

$$\rho_f = \rho_{\text{refi}} \left(1 + \left(P - \left(\frac{\alpha_i}{\beta_i}\right)(T - T_{\text{ref}})\right) k_i \beta_i\right)^{\frac{1}{k_i}}, \tag{5}$$

ρ_f and ρ_{refi} are the final and reference density for each composition at reference temperature ($T_{\text{ref}} = 293$ K) and surface pressures. P is the total pressure, α_i is the thermal expansivity, β_i is the isothermal compressibility and k_i is the isothermal bulk-modulus pressure derivative.

The dominant mechanism of deformation depends on the yield stress, which is equivalent to the maximum deviatoric stress that a rock is able to withstand without experiencing permanent deformation in steady-state (Goetze & Evans, 1979). When the second invariant of the deviatoric stress is higher than the yield stress, the plastic (brittle) deformation is described by the Drucker-Prager criterion (Equation 6).

$$\text{in 3D} : \sigma y = \frac{6\text{C} \cdot \cos\Phi}{\sqrt{3}(3 - \sin\Phi)} + \frac{6\text{P} \cdot \sin\Phi}{\sqrt{3}(3 - \sin\Phi)}, \tag{6}$$

where C, P and ϕ hold for the cohesion, pressure, and the internal friction angle (radians), respectively. Additionally, we included a linear plastic strain softening for the crustal layers which depends on the integrated strain accumulation (Table S1 in Supporting Information S1), however mostly ineffective because of the short model time (Figure S1 in Supporting Information S1). The effective plastic viscosity (Equation 7) is given by:

$$\eta = \frac{\sigma y}{2\dot{\varepsilon}}, \tag{7}$$

Where $\dot{\varepsilon}$ is the square root of second invariant of the strain rate. When the second invariant of the deviatoric stress is lower that the yield stress, viscous (ductile) deformation is simulated by harmonic averaging of dislocation and diffusion-creep mechanisms (Equation 8, Glerum et al., 2018):

$$\eta_{\text{diff|disl}} = 0.5\, A_{\text{diff|disl}}^{\left(-\frac{1}{n}\right)} d^m \dot{\varepsilon}^{\frac{1.-n}{n}} \exp\left(\frac{Q_{\text{diff|disl}} + P \cdot V_{\text{diff|disl}}}{nRT}\right), \tag{8}$$

where A is the prefactor rescaled from uniaxial experiments, n is the stress exponent, d and m are the grain size and grain size exponent, Q is the energy of activation, V is the volume of activation, P the pressure, R the gas

19449194, 2023, 8, Downloaded from https://agupubs.onlinelibrary.wiley.com/doi/10.1029/2023TC007765 by Rwth Aachen Hochschulbibliothe, Wiley Online Library on [15/01/2024]. See the Terms and Conditions (https://onlinelibrary.wiley.com/terms-and-conditions) on Wiley Online Library for rules of use; OA articles are governed by the applicable Creative Commons License

constant, and T the temperature. Dislocation creep is grain-size independent, therefore the term d^m is removed from Equation 8 for η_{disl}. Symbols and units of the parameters used in the equations are summarized in Table S2 in Supporting Information S1.

The material and temperature fields used as input were defined on the basis of 3D lithospheric-scale models of the SCA (Rodriguez Piceda et al., 2021; Rodriguez Piceda, Scheck-Wenderoth, Bott, et al., 2022) and are described along with the mechanical properties corresponding to the lithospheric layers in Section 2.2. Since each conservation equation is solved together using the continuity equation, the deformation takes the appearance of shear zones in numerical geodynamic modeling. Therefore, highly deformed areas potentially represent highly "faulted areas."

2.2. Model Setup

The geometries of the lithospheric layers were adopted from the 3D structural model of Rodriguez Piceda et al. (2021). This model is built upon the integration of geophysical and geological data and models, including the gravity field, and covers a region of 700 km × 1,100 km × 200 km (Figure 1). Eight layers constituting the model were defined based on the principal density contrasts in the lithosphere (1–2) oceanic and continental sediments ("sediments," Figure 2a); (c) upper continental crystalline crust ("upper crust," Figure 2c); (d) lower continental crystalline crust ("lower crust," Figure 2d); (e) continental lithospheric mantle ("continental mantle," Figure 2f); (f) oceanic crust; (g) oceanic lithospheric mantle ("oceanic mantle"), and (h) asthenospheric mantle. For the geodynamic simulations, two main modifications were introduced to change the original model of Rodriguez Piceda et al. (2021). First, the model was extended 200 km in depth, 500 km in the E-W direction, and 200 km in the N-S direction. The resulting box model is 1,700 × 1,700 × 400 km, with a central area of interest of 600 × 600 × 400 km (Figure 3a). Second, we introduced an interface representing the lithosphere-asthenosphere boundary (LAB) in the continental plate based on the thermal LAB model of Hamza and Vieira (2012). The main features of the model are depicted (Figure 2) in terms of the: (a) thickness of sediments; (b) thickness of the continental crust; (c) thickness of the upper crust; (d) thickness of the lower crust; (e) Moho depth, and (f) LAB depth.

We defined the initial temperature field as deduced from the 3D thermal model of the SCA of Rodriguez Piceda, Scheck-Wenderoth, Bott, et al. (2022), over the same area defined by the structural model of Rodriguez Piceda et al. (2021). Temperatures were derived from the conversion of S-wave tomography (Assumpção et al., 2013) together with steady-state conductive modeling, and were additionally validated by borehole temperatures and surface heat flow data (Rodriguez Piceda, Scheck-Wenderoth, Bott, et al., 2022). One caveat of this model is related to the determination of the thermal structure of the oceanic slab through the conversion of S-wave tomography to temperature. The lack of seismic tomography resolution (0.5° longitudinally and 25 km in depth) does not allow us to properly resolve the oceanic plate thermal state, which results in relatively high temperatures in comparison to the temperatures predicted by numerical solutions (van Keken et al., 2019; Wada & Wang, 2009). For this reason, we have assigned a conductive geotherm between 273 and 1573 K from the top to the base of the oceanic plate as initial condition.

The thermomechanical properties of each model unit were assigned according to its lithological composition (Rodriguez Piceda et al., 2021; Rodriguez Piceda, Scheck-Wenderoth, Bott, et al., 2022). These lithologies were inferred from the comparison between gravity-constrained densities (Rodriguez Piceda et al., 2021) and mean P-wave velocities (Araneda et al., 2003; Contreras-Reyes et al., 2008; Marot et al., 2014; Pesicek et al., 2012; Scarfi & Barbieri, 2019), combined with rock-properties compiled from literature (Brocher, 2005; Christensen & Mooney, 1995; Sobolev & Babeyko, 1994) and other seismic properties (Alvarado et al., 2007; Ammirati et al., 2013, 2015, 2018; Gilbert et al., 2006; Wagner et al., 2005). The reference density for each composition was recalculated to ensure that: (a) the estimated final density of each composition (i.e., after correcting for pressure and temperature, Equation 5, Table S1, Figure S2 in Supporting Information S1), is in the range of the density predicted by the structural model of Rodriguez Piceda et al. (2021), and (b) the resulting topography does not deviate substantially from the present-day topography (Text S1 in Supporting Information S1 and Figure 1). The thermal properties used in the initial thermal field are from published average values for the lithology of each model unit (see references in Rodriguez Piceda, Scheck-Wenderoth, Bott, et al., 2022).

We assigned rheological properties to each of the eight compositions that define the model: dry olivine (Hirth & Kohlstedt, 2004, H&K2004) to the oceanic mantle lithosphere (3,321 kg/m³), diabase (Mackwell et al., 1998,

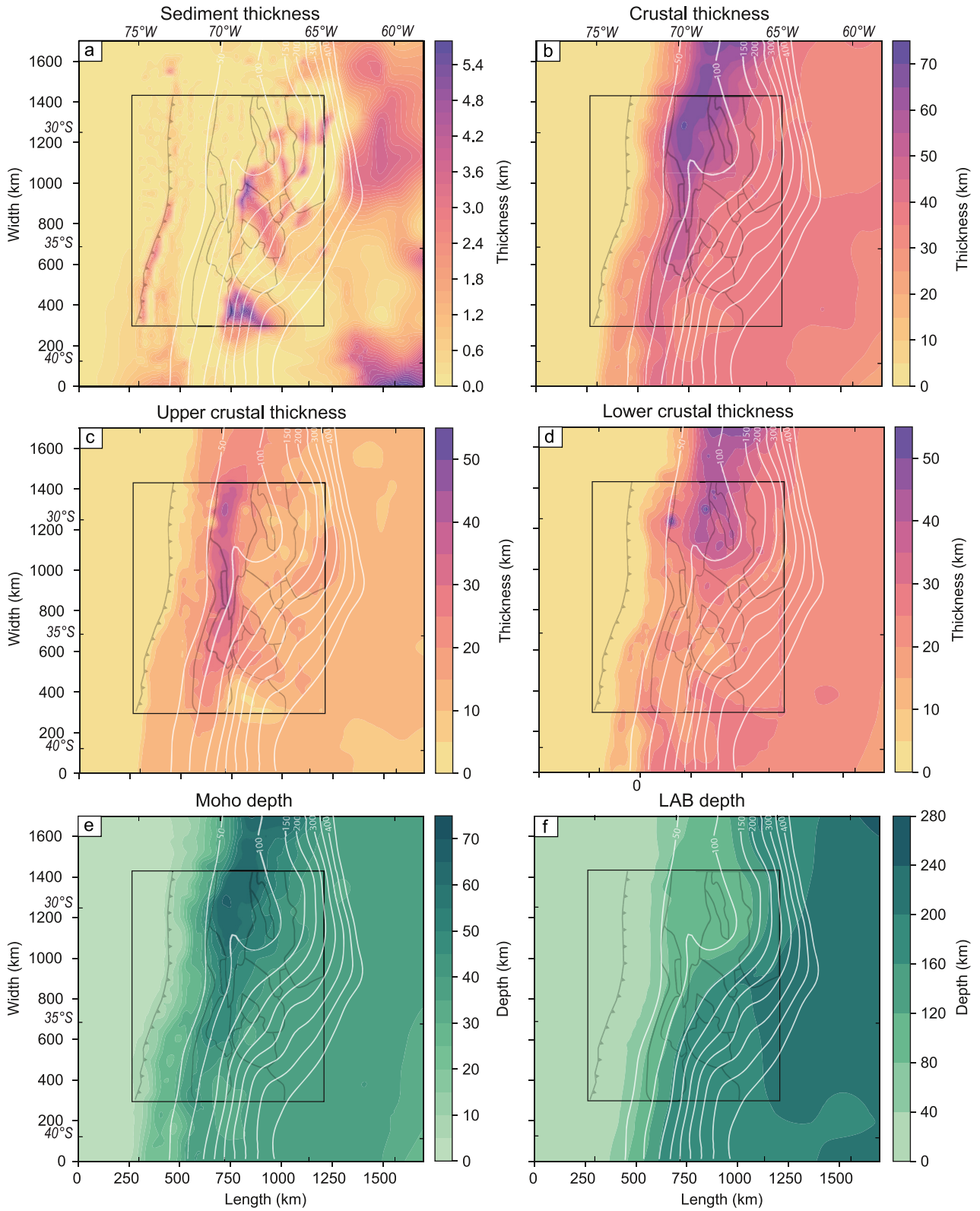


Figure 2. Layer thickness and depth map of the SCA. Main structural features of the SCA lithosphere from the model of Rodriguez Piceda et al. (2021). (a) sediment thickness; (b) total crystalline crustal thickness; (c) upper continental crustal thickness; (d) lower continental crustal thickness; (e) Moho depth and (f) LAB depth taken from Hamza and Vieira (2012). The black rectangle shows the most refined model area.

19449194, 2023, 8, Downloaded from https://agupubs.onlinelibrary.wiley.com/doi/10.1029/2023TC007765 by Rwth Aachen Hochschulbibliothe, Wiley Online Library on [15/01/2024]. See the Terms and Conditions (https://onlinelibrary.wiley.com/terms-and-conditions) on Wiley Online Library for rules of use; OA articles are governed by the applicable Creative Commons License

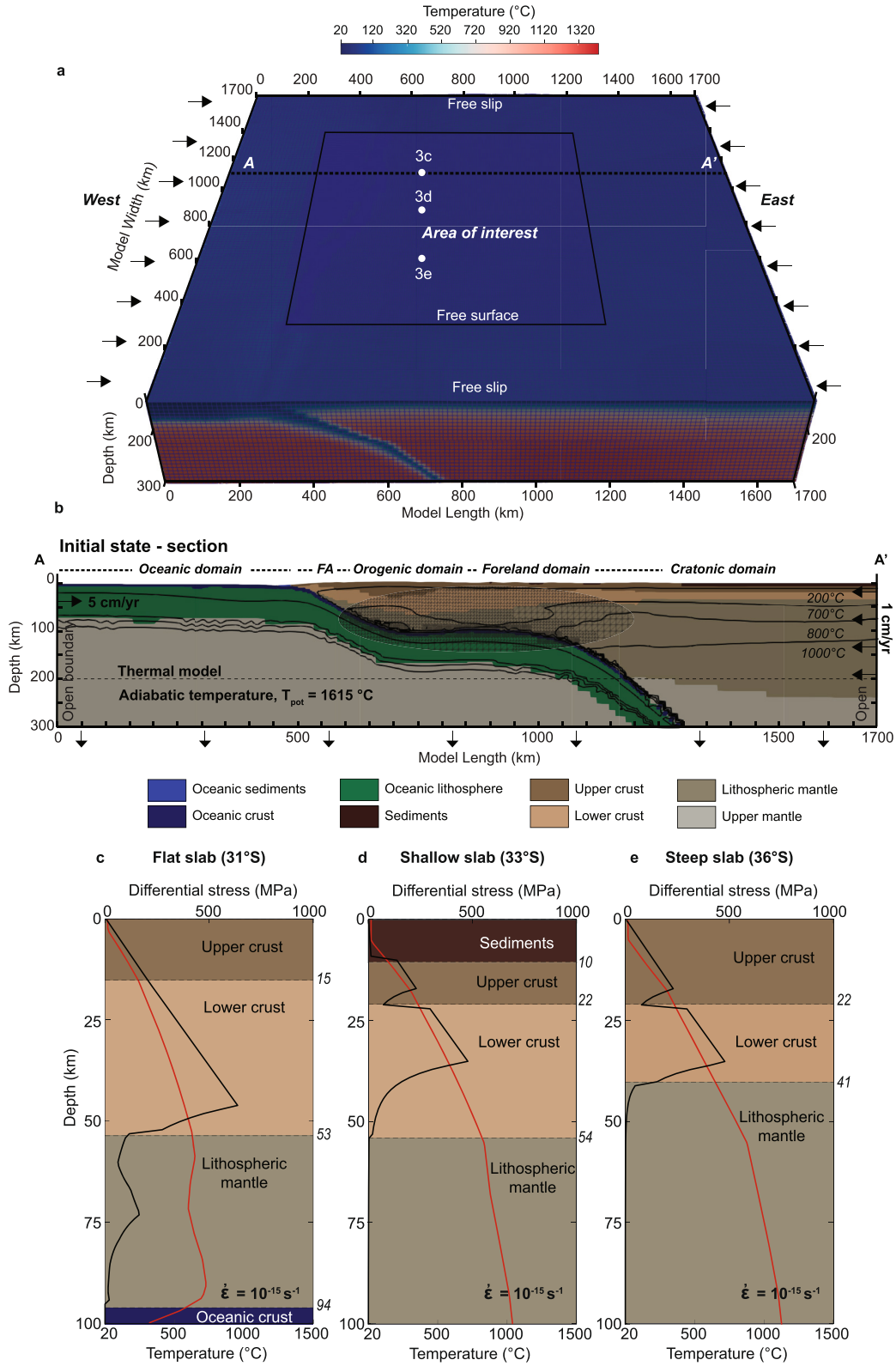


Figure 3. Model setup. (a) 3d model geometry, mesh refinement with areas of higher resolution and temperature. (b) 2D W-E cross section along with location indicated in (a), showing boundary and initial conditions, refinement of the interface, composition of the lithospheric layers, and temperature. T_{pot} indicates the mantle potential temperature and FA the forearc domain. (c–e) yield strength (black line) and temperature (red line) profiles of the upper plate at: (c) flat-slab. (d) shallow slab. (e) steep slab derived from the thermal model of Rodriguez Piceda, Scheck-Wenderoth, Bott, et al. (2022).

19449194, 2023, 8, Downloaded from https://agupubs.onlinelibrary.wiley.com/doi/10.1029/2023TC007765 by Rwth Aachen Hochschulbibliothe, Wiley Online Library on [15/01/2024]. See the Terms and Conditions (https://onlinelibrary.wiley.com/terms-and-conditions) on Wiley Online Library for rules of use; OA articles are governed by the applicable Creative Commons License

19449194, 2023, 8, Downloaded from https://agupubs.onlinelibrary.wiley.com/doi/10.1029/2023TC007765 by Rwth Aachen Hochschulbibliothe, Wiley Online Library on [15/01/2024]. See the Terms and Conditions (https://onlinelibrary.wiley.com/terms-and-conditions) on Wiley Online Library for rules of use; OA articles are governed by the applicable Creative Commons License

Mck1998) to the lower crust (3,129 kg/m³), wet olivine (Hirth & Kohlstedt, 2004) to the continental mantle lithosphere (3,388 kg/m³), wet quartzite (Gleason & Tullis, 1995, G&T1995) to the upper crust (2,812 kg/m³), the oceanic and continental sedimentary layer (2,300 and 2,400 kg/m³), and wet olivine (Hirth & Kohlstedt, 2004) to the upper asthenospheric mantle to represent the hydrated mantle wedge.

For the oceanic crust (2,857 kg/m³), we prescribed a weak quartzite rheology (Ranalli, 1997) to simulate the visco-plastic behavior of a quartz-dominated "mélange," which is characteristic of the subduction interface (Gerbault et al., 2009; Muldashev & Sobolev, 2020; Sobolev et al., 2006), with a relatively low friction coefficient of 0.015. This setup produces an appropriate maximum shear stress of 20–40 MPa (Lamb & Davis, 2003; Sobolev et al., 2006; G. Yáñez & Cembrano, 2004), depending on the temperature and the dip of the oceanic plate (Figure S3 in Supporting Information S1).

For the plastic regime, we set a cohesion of 40 MPa and a friction angle of 30° to the mantle layers. The short model runtime prevents the layers from weakening by accumulating plastic strain, thus we assigned a weak plastic rheology to the sedimentary layer (i.e., a friction angle of 3° and a cohesion of 2 MPa). The minimum viscosity was set to 1e19 Pas during the first 100 ka of model run, to dampen any excessive velocities that could result from the isostatic equilibrium of the expanded model areas (Figure S4 in Supporting Information S1). Once the model reached isostatic equilibrium, the minimum viscosity was changed to 2.5e18 Pas in order to more accurately represent the range of values estimated for subduction zones (Figure S5 in Supporting Information S1), including low viscosities representative of the hydrated mantle wedge corner (Hirth & Kohlstedt, 2003). Yield strength profiles representative of the different subduction segments are shown in Figures 3d and 3e. Here, we refer to the second invariant of the square root of the deviatoric strain rate in the plastic and viscous domains as plastic strain rate and viscous strain rate for the visualization, respectively. We used adaptive mesh refinement (Figures 3a and 3b) to resolve the central, outer domains and subduction interface, with a resolution of ∼6km and ∼12.5 km and ∼3 km, respectively. We ran the model simulation for ∼250 ka while applying velocities of 5 cm/yr and 1 cm/yr to the oceanic and continental plates, respectively (Sdrolias & Müller, 2006), whereas the left and right asthenosphere borders were left open. Since the lithospheric and structural model implemented in our geodynamic model is already near equilibrium in a steady-state stress regime, only minor isostatic adjustments are needed for the extended areas introduced in this study (Figures S4, S6, S7 in Supporting Information S1). It takes 100,000 years to reach equilibrium in these additional areas. Prescribed velocities were applied at the eastern and western boundaries, perpendicular to the trench, thus deformation localized at the surface within a relatively short period of less than 150,000 years (Figure S7 in Supporting Information S1). Similar time settings were employed in previous studies to obtain quasi-instantaneous solutions (Glerum et al., 2020, 2021; Ibarra et al., 2019). We prescribed an equivalent volume outflow to the bottom boundary equal to the prescribed inflow from the plate velocity (Figure 3a). At the northern and southern boundaries, free-slip conditions were applied (Figure 3a). We used the advantages of the ASPECT code by prescribing a dynamically deformable mesh in order to simulate present-day topography. In particular, the model topography is uplifted and advected using the ASPECT-FastScape coupling (Bovy, 2021; Braun & Willett, 2013; Neuharth et al., 2021).

First, we computed the reference model (S1) using the parametrization discussed above (Section 2.2). Subsequently, we ran a series of models (S2, S3, S4 and S5, Table 1) with varying multiple parameters to investigate the relative contribution of key factors with respect to the strain localization in the upper plate.

3. Modeling Results

3.1. Reference Model (S1)

Reference model S1 is built upon known values for plate convergence, subduction-interface friction coefficient, sediment strength, and present-day topography (see Methods section and Table S1 in Supporting Information S1). Plastic deformation within the model, resulting in the generation of shear zones (faults), is equivalent to brittle deformation. From south to north, deformation migrates to the east, with strain localizing in the southern part, while in the northern part it is distributed over multiple faults with a length of 200–400 km and a depth of 40–50 km (Figures 4 and 5). This shift is related to a transition between two distinct foreland shortening modes: simple and pure shear modes (Figure 5). Pure-shear shortening involves uniform vertical thickening of the crust, resulting in distributed deformation characterized by multiple steep faults within the crystalline basement (thick-skin deformation style). In the model, this occurs where high plastic strain is disconnected from high viscous

19449194, 2023, 8, Downloaded from https://agupubs.onlinelibrary.wiley.com/doi/10.1029/2023TC007765 by Rwth Aachen Hochschulbibliothe, Wiley Online Library on [15/01/2024]. See the Terms and Conditions (https://onlinelibrary.wiley.com/terms-and-conditions) on Wiley Online Library for rules of use; OA articles are governed by the applicable Creative Commons License

Table 1
Model Variations With Respect to the Reference Model

Tested parameters	Name	Variation
Friction coefficient of the subduction interface (μ_{int})	S2a	$\mu_{int} = 0.005$
	S2b	$\mu_{int} = 0.035$
	S2c	$\mu_{int} = 0.05$
	S2d	$\mu_{int} = 0.07$
Sediment strength (internal friction angle Φ and cohesion C)	S3a	$\Phi = 30°, C = 20$ MPa
	S3b	$\Phi = 30°, C = 2$ MPa
	S3c	$\Phi = 15°, C = 20$ MPa
	S3d	$\Phi = 3°, C = 20$ MPa
Variation of topography and boundary velocity (no initial topography prescribed)	S4a	Free surface (advection of topography allowed), with boundary velocity
	S4b	Free surface (advection of topography allowed), with no boundary velocity
	S4c	Free slip (no advection of topography allowed), with boundary velocity
	S4d	Free slip (no advection of topography allowed), with no boundary velocity
Velocities of the subducting plate (SP) and the overriding plate (OP)	S5a	SP = 0 cm/yr OP = 1 cm/yr (Absolute velocity orthogonal to the trench)
	S5b	SP = 5 cm/yr (Absolute velocity orthogonal to the trench) OP = 0 cm/yr
	S5c	SP = 6 cm/yr OP = 0 cm/yr (Convergence velocity)
	S5d	SP = 0 cm/yr OP = 6 cm/yr (Convergence velocity)

strain beneath (Figure 5a). Simple-shear shortening produces asymmetric crustal thickening, often involving the underthrusting of the foreland lithosphere beneath the orogenic lithosphere along a shallow décollement. This shortening is associated with a thin-skin deformation style, where the sedimentary cover is deformed while the basement is relatively less deformed. The term "less deformed" (also seen in the literature, e.g., Dahlen, 1990; Lacombe & Bellahsen, 2016; Pfiffner, 2017) refers to the involvement of fewer basement faults in the thin-skin style, although it corresponds to a greater amount of shortening compared to the thick-skin style. In the model, the existence of a pure-shear shortening mechanism is identified when regions of high plastic strain in the upper crust connect at depth with areas of high viscous strain in the lower crust, forming an asymmetric shear zone (Figures 5c and 5d). The resulting surface strain-rate field indicates three distinct north-to-south oriented branches (Figure 4a) characterized by a distinct shortening mode:

1. A Western branch (75°–73°W, 29°–39°S), which corresponds to the trench. Here, both plates are decoupled by the weak subduction interface, where most of the deformation localizes along a N-S elongated (~1,000 km) and 60 to 80-km-deep area (Figures 4a and 5a–5c). Conversely, the crust of the adjacent cold and mechanically strong forearc is virtually undeformed.
2. An Eastern branch (60°–65°W, 27°–41°S), where deformation localizes in front of the flat slab by pure-shear shortening, as well as along regions that spatially correlate with pre-Andean basement hetereogeneities related to the amalgamation of terranes during the formation of Gondwana, such as the Transbrazilian Lineament (Fairhead & Maus, 2003; Ramos, 2010). In the south, deformation localizes within smaller structures that straddle the Rio de la Plata craton. The N-S extent of this area is 1,600 km and the depth is 50 km (Figures 4a and 5a–5c).
3. A Central branch (65°–70°W, 31°–41°S), which comprises the orogen and the adjacent foreland. Strain distribution varies from north to south. In the flat-slab segment, the strain localizes at the eastern front of the orogen

10.1029/2023TC007765

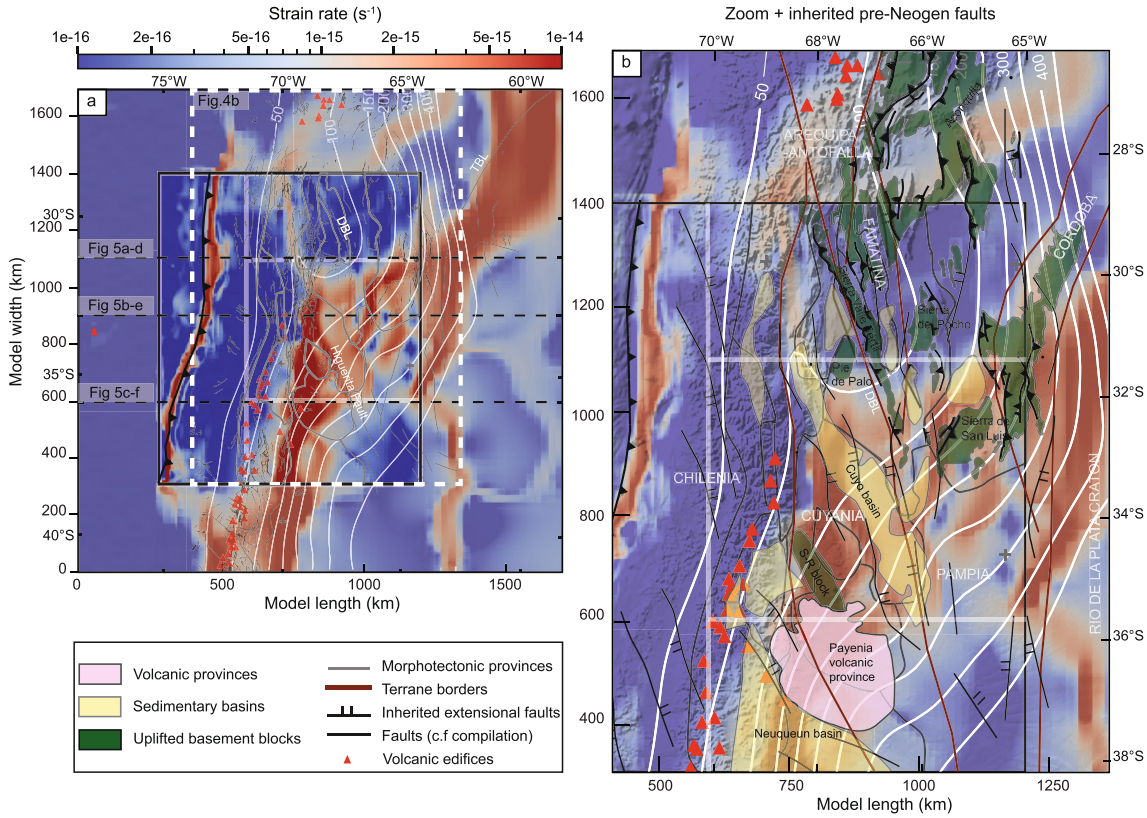


Figure 4. Surface-strain rate of the reference model. (a) Strain rate superposed with compiled faults (Broens & Pereira, 2005; Costa et al., 2020; Eisermann et al., 2021; Folguera & Zárate, 2011; García, 2001; Giambiagi et al., 2003; Jensen, 2018; Litvak et al., 2018; Martínez et al., 2017; Martino et al., 2016; Meeßen et al., 2018; Melnick et al., 2020; Moscoso & Mpodozis, 1988; Olivar et al., 2018; Riesner et al., 2018). (b) Close-up of the Sierras Pampeanas morphotectonic province and extensional faults and terrane sutures in red (Ramos et al., 2002; Wimpenny, 2022). Green structures indicate uplifted Sierras Pampeanas ranges. White lines are isobaths of the top of the subducting oceanic plate. Red triangles indicate the position of known volcanic edifices. Major structures and morphotectonic provinces are highlighted by different colors in the legend.

and intensifies southward and the foreland crust is almost undeformed. In the shallow-slab segment, the strain distributes in the foreland over multiple oblique or en-échelon, crustal-scale structures that connect to the Eastern branch and which are associated with pure-shear shortening. The N-S extent of this region is 600 km (Figure 4a), and the depth of the structures is between 40 and 45 km (Figure 5b). In the steep-slab segment, strain localizes in front of the orogen and in the foreland by simple-shear shortening over a structure that is 600 km long in N-S direction (Figure 4a) and at a depth of ~80 km (Figure 5c).

On a lithospheric scale, these three branches interact spatially. The Sierras Pampeanas morphotectonic province appears as a large-scale transpressional dextral shear zone that accommodates deformation via en-échelon structures associated with the uplift of isolated basement blocks (Figure S7 in Supporting Information S1). The deformation at the borders of these uplifts is accommodated by diffuse dextral strike-slip deformation as well as rigid block rotation (Figure S7 in Supporting Information S1).

We also distinguish that the deformation localizes differently along the three slab segments of the subducting Nazca Plate (Figure 5): the flat segment (27° to 32°S, 1,000–1,400 km model width-coordinates), the shallow segment (32° to 35°S, a 600–1,000 km model width coordinates), and the steep segment (35° to 41°S, 0–600 km model width coordinates). The E-W-oriented cross sections across the reference model (Figure 5) illustrate how plastic (brittle) and viscous deformation is accommodated in the continental plate along the segments with different slab geometry (Figures 5a–5c), and how stresses are distributed within the plates (Figures 5d–5f, Figures S8–S12 in Supporting Information S1). Above the steep segment, the upper plate is characterized by simple-shear shortening at the front of the orogenic thrust wedge (Figure 5c, Figure S10 in Supporting Information S1). Above the shallow subduction segment, the model predicts a mixture of simple and pure-shear shortening (Figure 5b,

19449194, 2023, 8, Downloaded from https://agupubs.onlinelibrary.wiley.com/doi/10.1029/2023TC007765 by Rwth Aachen Hochschulbibliothek, Wiley Online Library on [15/01/2024]. See the Terms and Conditions (https://onlinelibrary.wiley.com/terms-and-conditions) on Wiley Online Library for rules of use; OA articles are governed by the applicable Creative Commons License

10.1029/2023TC007765

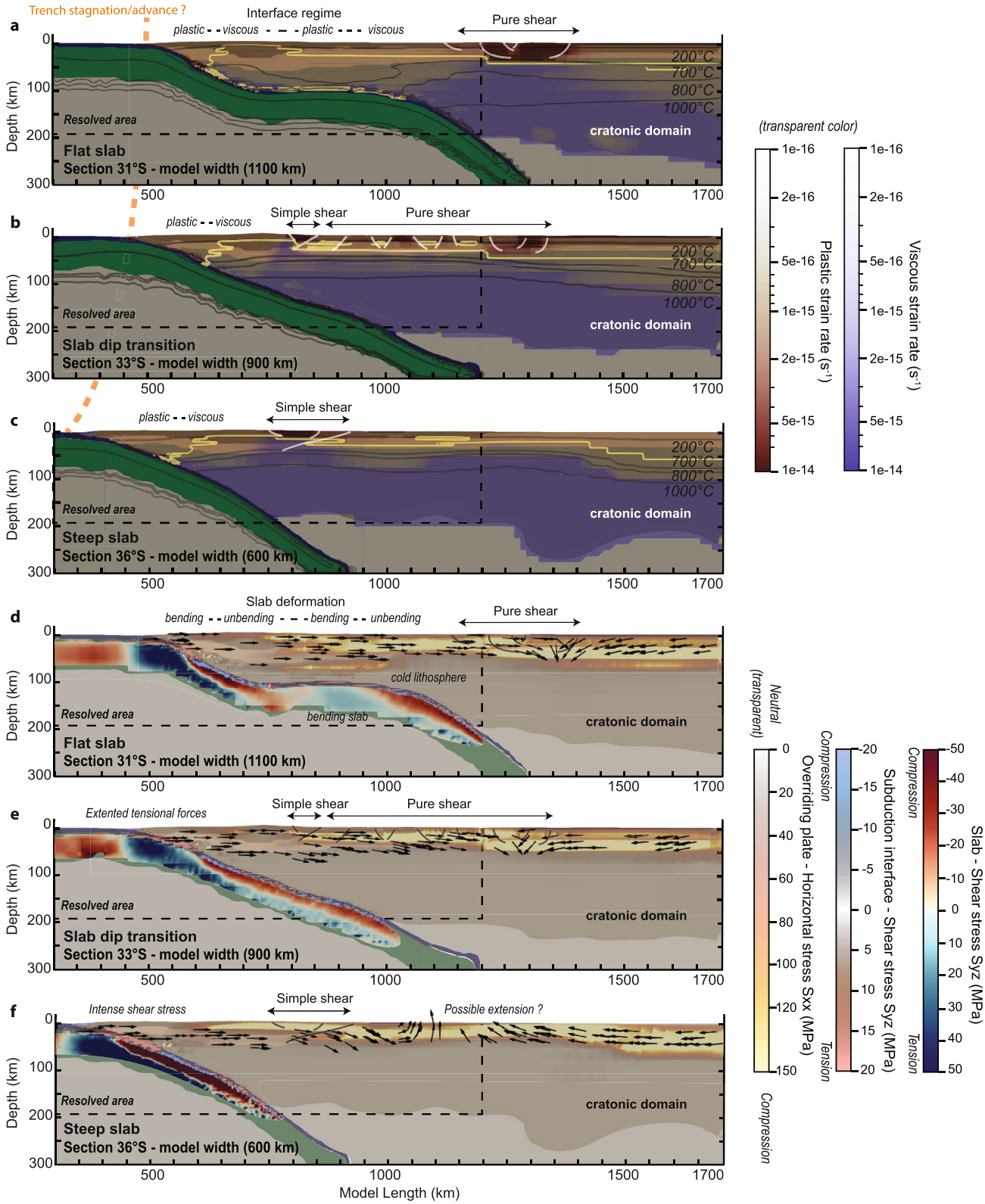


Figure 5. Representative cross sections of the subduction segments for the reference model after 250 kyr of simulation time (see location in Figure 1): Strain rate (a–c) and stress (d–f). (a–d) Flat-slab (31°S). (b–e) Shallow slab (33°S) and (c–f) Steep slab (36°S). In panels (a–c) white lines are interpreted faults, yellow lines show the depth of the brittle-ductile transition (BDT), and dark lines indicate isotherms. Panels (d–f) black lines indicate the interpreted faults, arrows indicate the sense of the velocity for the crust.

19449194, 2023, 8, Downloaded from https://agupubs.onlinelibrary.wiley.com/doi/10.1029/2023TC007765 by Rwth Aachen Hochschulbibliothe, Wiley Online Library on [15/01/2024]. See the Terms and Conditions (https://onlinelibrary.wiley.com/terms-and-conditions) on Wiley Online Library for rules of use; OA articles are governed by the applicable Creative Commons License

19449194, 2023, 8, Downloaded from https://agupubs.onlinelibrary.wiley.com/doi/10.1029/2023TC007765 by Rwth Aachen Hochschulbibliothe, Wiley Online Library on [15/01/2024]. See the Terms and Conditions (https://onlinelibrary.wiley.com/terms-and-conditions) on Wiley Online Library for rules of use; OA articles are governed by the applicable Creative Commons License

Figure S11 in Supporting Information S1). No significant deformation occurs above the flat-slab segment, while pure-shear deformation takes place at its eastern edge (Figure 5a).

The greatest horizontal stress is transmitted efficiently throughout the continental plate to weak regions where the deformation localizes (Figures 5d–5f, Figures S9–S12 in Supporting Information S1). In the flat-slab section (Figure 5a, Figure S11 in Supporting Information S1), deformation takes place more than ∼700 km away from the trench and is localized over a 200-km-wide band in the eastern broken foreland of the Sierras Pampeanas. The model predicts local plastic deformation (Figure 5a) on top of the colder flat-slab segment at 100 km depth (Figure 5c, Figure S12 in Supporting Information S1), which also correlates with the bending of the slab (Figures 5a and 5d). Horizontal stresses of >200 MPa are generated locally in the continental crust and in the colder lithospheric mantle of the forearc, where the brittle-ductile transition (BDT) is deeper and where the deviatoric stress is locally more than 300 MPa (Figure S13 in Supporting Information S1). Consequently, horizontal stresses are not sufficiently large to cause significant deformation. The thick and warmer orogen shows no significant deformation despite being weaker, which is illustrated by the shallower BDT (Figure 5a). On top of the flat-slab segment, the greatest horizontal stress is mainly generated by the subducting plate as shown by the eastward-pointing velocity vectors (Figure 5d, Figure S6 in Supporting Information S1). The horizontal stresses also build up within the cold and strong lithospheric mantle of the foreland (Figure S12 in Supporting Information S1). Despite the presence of a weak sedimentary basin at the surface, deformation does not localize, and stresses are transmitted eastward from the base of the upper crust to the eastern Sierras Pampeanas. Finally, crustal shortening results in a stress drop in the eastern Sierras Pampeanas, and the polarity of the velocity field switches from east to west in the reference model (Model S1), indicating that velocity is now determined by the upper plate (Figure 5d, Figure S6 in Supporting Information S1).

In the shallow-slab section (Figure 5b), the plastic and viscous strain rates merge in front of the orogen (at ∼800 km model coordinates) to form a deep shear zone dominated by simple-shear shortening. In the foreland, the deformation distributes over multiple faulted areas along a wide area, with rigid crustal blocks characterized by a shallower BDT. Similar to the previous section, in the shallow slab section deformation terminates in the transition with the cratonic domain and is characterized by a thick-skinned style, which results from pure-shear shortening. The horizontal stress also builds up locally in the cold forearc (>∼200 MPa; Figure 5e, Figure S11 in Supporting Information S1), where the greater mechanical strength of the rocks prevents failure and causes a transmission of stresses toward the orogen. Additionally, the horizontal stress builds up in the lower crust and is partially transmitted to the eastern Sierras Pampeanas. Strain localizes at the orogenic front by simple-shear shortening and is accommodated by pure-shear shortening in the foreland and at the transition with the cratonic domain. This interpretation arises from the symmetry observed in the strained area and the fact that it experiences exclusively high plastic strain rates. In the steep-slab section, the deformation strongly localizes in front of the orogen (∼800 km model length; Figure 5c, Figure S10 in Supporting Information S1).

3.2. Model Variations

In this section, we tested the relative contribution of four key parameters on the resulting surface strain-rate distribution: (a) the friction coefficient at the oceanic plate interface; (b) the strength of continental sediments; (c) the topography; and (d) the velocity applied to the model boundaries. The friction coefficient at the oceanic plate interface is varied between 0.005 and 0.05 (Models S2a–c) in agreement with the models of the long-term evolution of the Central Andes (Gerbault et al., 2009; Sobolev & Babeyko, 2005; Sobolev et al., 2006). The internal friction angle (Φ) and cohesion (C) of the sediments is varied from 3° to 30° (friction coefficient 0.05 to 0.5) and from 2 to 20 MPa, respectively (Figure 6 and Figure S14 in Supporting Information S1, Models S3a–d). In addition, we tested the effect of topography on the strain distribution by removing the topographic relief in the initial configuration with and without applied velocities at the boundaries (Figure 6 and Figure S14 in Supporting Information S1, Models S4a–d). Finally, the oceanic and continental plate velocities are varied between 0 and 6 cm/yr, covering the range of possible velocities over the last ∼20 Ma (Figure 6 and Figure S14 in Supporting Information S1, Models S5a–d). Table 1 summarizes the alternative model runs and Figure S14 in Supporting Information S1 shows the strain rate distribution of the various alternative models. In order to discuss the relative effect of each key parameter on the strain localization we computed the residual surface strain rate between the model variant and the reference model (Figure 6). To estimate the variation in strain localization in the trench, and the flat, shallow, and steep subduction segments, we subdivided the surface of each model into domains

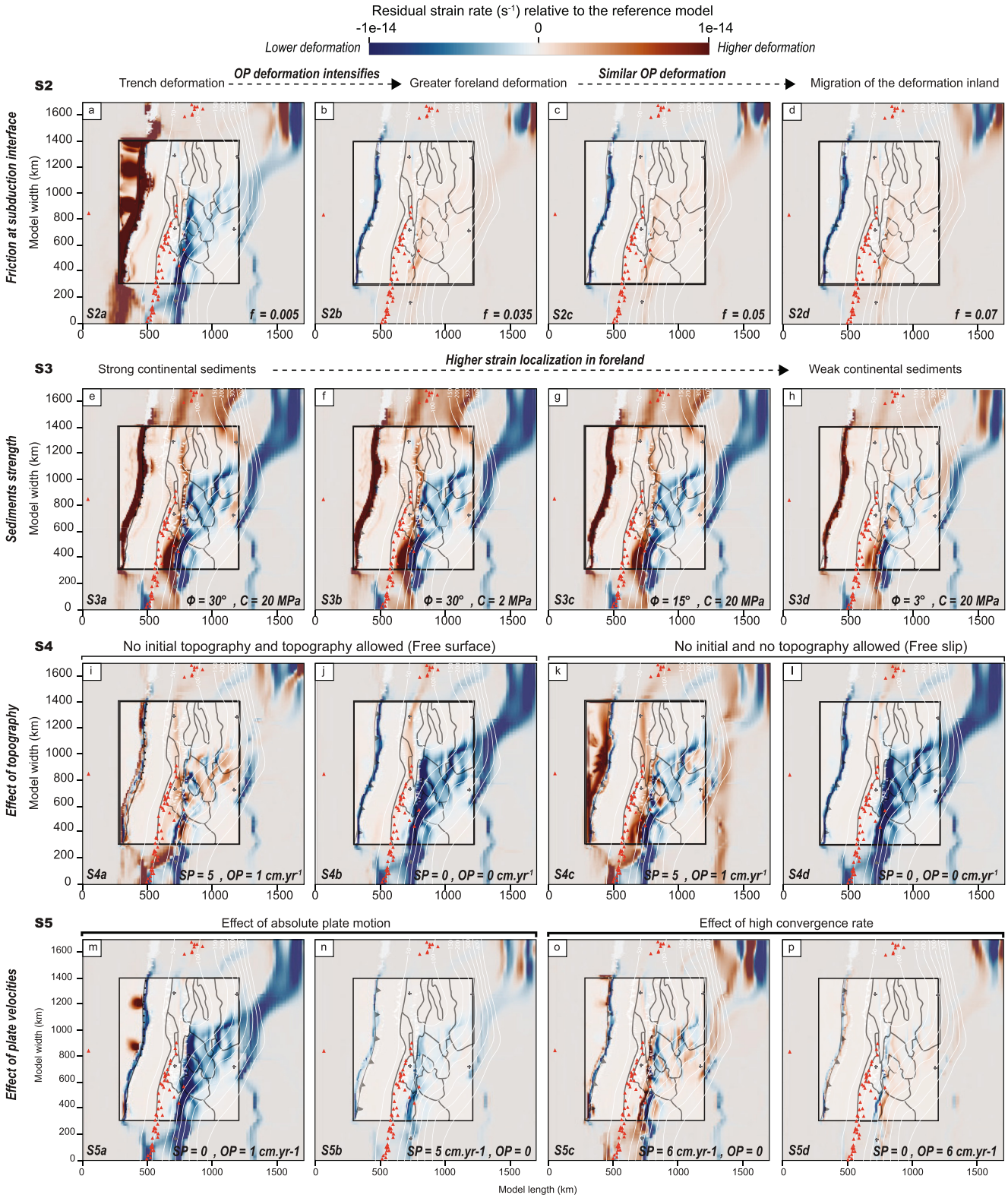


Figure 6.

19449194, 2023, 8, Downloaded from https://agupubs.onlinelibrary.wiley.com/doi/10.1029/2023TC007765 by Rwth Aachen Hochschulbibliothe, Wiley Online Library on [15/01/2024]. See the Terms and Conditions (https://onlinelibrary.wiley.com/terms-and-conditions) on Wiley Online Library for rules of use; OA articles are governed by the applicable Creative Commons License

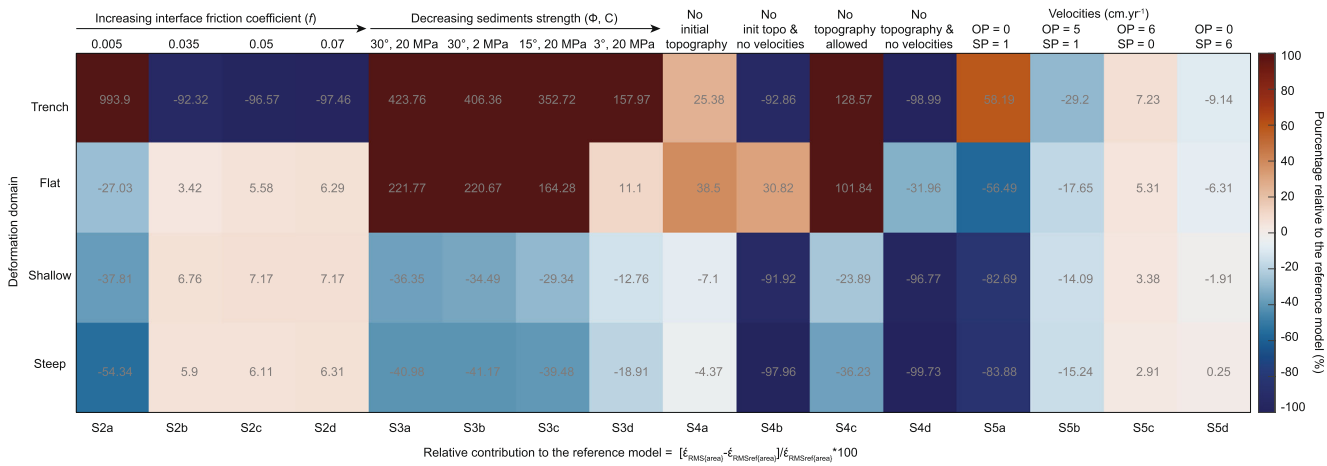


Figure 7. Relative surface strain-rate difference between the reference and the model variants. Relative change of strain rate in percentage $[\acute{\varepsilon}\mathrm{RMS}(\mathrm{area}) - \acute{\varepsilon}\mathrm{RMSref}(\mathrm{area})] / \acute{\varepsilon}\mathrm{RMSref}(\mathrm{area}) * 100$ with respect to the reference model in each deformation domain for each model variant.

corresponding to these segments. For each domain, we calculated an average of the surface strain rate using the root mean square. Finally, we calculated the relative change between the domains of the model variants and of the reference model. Thus, we obtained a summary of the relative percentage of contribution of each key parameter to the reference model for each domain (Figure 7). Note that for a similar force budget between the reference model and the model variants we would expect that if the strain localizes further in one of the branches (Section 3.1), it may decrease in another one to keep a shortening balance. However, because part of the deformation might be redistributed outside of the area of interest or be partitioned over the latitude, the sum of the relative percentage of deformation of each domain (Figure 7) might not be equal to 0%.

3.2.1. Models With Variable Slab-Interface Friction (S2a–d)

The greatest differences between the reference and alternative models related to the slab interface friction occurs along the trench (Figure 6 and Figure S14 in Supporting Information S1). With low slab interface friction (S2a; Figure 6a), the strain strongly localizes more at the trench (×18 or +994%, Figure 7). Less strain localizes within the overriding plate (−27% to −54%), including the orogen and the back-arc. Conversely, higher interplate friction (S3b–c; Figures 6b–6d) translates into lower strain localization at the trench (−92% to 97%), and slightly higher overriding plate deformation (+6%, Figure 7). Therefore, for these short-timescale simulations the increase of friction at the interface results in similar intensity of upper-plate deformation with respect to the reference Model S1.

3.2.2. Strength of Continental Sediments (S3a–d)

Modifying sediment strength results in a significant change in strain-rate distribution. Weaker sediments lead to a higher degree of strain localization adjacent to the orogen and the foreland basins (S3a–d, Figures 6e–6h). A decrease in the internal friction angle (S3c and S3d, Figures 6f and 6h) decreases the strength significantly more than a decrease in their cohesion (S3b and S1, Figures 6g and 4), promoting the compressional reactivation of foreland structures. However, near the surface, the effect of friction becomes negligible and sediment strength depends mainly on cohesion (Section 2.1, Equation 6). Consequently, for the same sediment cohesion but different frictions, strain localization at the surface may vary due to the variation of strength of sediments at deeper locations. With high friction and cohesion (S3a, Figure 6e), the strain rate in the foreland appears to be more diffuse and less localized (−35% and −40%), causing strain to localize closer to the orogen and the trench

Figure 6. Residual strain-rate distribution obtained by subtracting the reference model S1 to the model variants. (a–d) Models with variable friction coefficients (f) at the subduction interface. (e–h) Models with alternative strength (Φ internal friction angle, and *C* cohesion) of the sedimentary layer. (e) S3a, $\Phi = 30°$, $C = 20$ MPa. (i–l) Models without prescribing initial topography. (m–p) Models with variations of prescribed velocities in the subducting (SP) and overriding (OP) plates. For a detailed description of each model variant, see Table 1. Black rectangle is the resolved area; dark line indicates the boundaries of the morphotectonic provinces, red triangles denote position of volcanic edifices. Sub-squares delimit the deformational domains (i.e., trench, flat subduction, shallow subduction and steep subduction) used to compute the strain-rate differences between the reference and model variants shown in Figure 7. Blue and red colors indicate smaller or higher rate of deformation than in the reference model, respectively.

19449194, 2023, 8, Downloaded from https://agupubs.onlinelibrary.wiley.com/doi/10.1029/2023TC007765 by Rwth Aachen Hochschulbibliothe, Wiley Online Library on [15/01/2024]. See the Terms and Conditions (https://onlinelibrary.wiley.com/terms-and-conditions) on Wiley Online Library for rules of use; OA articles are governed by the applicable Creative Commons License

19449194, 2023, 8, Downloaded from https://agupubs.onlinelibrary.wiley.com/doi/10.1029/2023TC007765 by Rwth Aachen Hochschulbibliothe, Wiley Online Library on [15/01/2024]. See the Terms and Conditions (https://onlinelibrary.wiley.com/terms-and-conditions) on Wiley Online Library for rules of use; OA articles are governed by the applicable Creative Commons License

(+220%) compared to the reference model (Figure 7). With weaker continental sediments, the major component of deformation switches from the orogen interior outward to the eastern front of the mountain belt. Overall, stronger sediments result in more active shallow deformation near the trench and in the orogen above the flat slab (S3a, 423%), and less pronounced deformation in the foreland above the shallower and steeper segments (~-40%, Figure 7).

3.2.3. Models With Topography Variations (S4a–d)

By initializing the model without present-day topography, we aim to look at the effect of internal forces related to the density and thickness configuration of the layers in the overriding plate. In models S4a and S4b, we allow for the topography to evolve with and without plate velocities, respectively (Figures 6i and 6j). S4a exhibits a strain-rate distribution similar to S1 (cf. Figure 6a), but with higher strain localization at the trench and in the orogen above the flat-slab (+25 and 38%, Figure 7). In S4b, although no horizontal velocity is prescribed, the strain rate is higher in the orogen above the flat slab (+30%) and lower elsewhere. To investigate the effect of topography on the strain distribution, we ran two alternative models inhibiting topographic growth, that is, with and without plate velocities (Models S4b–c; Figures 6j–6l). In the model with plate velocities (S4c) the strain rate is higher at the trench and the orogen on top of the flat slab (+128 and 101%), and it is more diffuse and lower in the foreland of the shallow and steep-subduction domains (−23% and −36%). Without plate velocities (S4d), the strain rate only localizes in a narrow corridor along the orogen and otherwise decreases elsewhere.

3.2.4. Velocity Boundary Conditions (S5a–d)

Varying the prescribed boundary velocity allows us to determine the contribution of each plate to the intensity of strain localization in the overriding plate. In model S5a (Figure 6m), where velocities are only prescribed to the overriding plate (1 cm yr^{-1}; Figure 6m), the intensity of deformation in the foreland is lower by 58%–83% in all domains compared to model S1 (Figure 7) because the deformation slightly localizes at the trench in specific places. In model S5b, where the overriding plate does not advance trenchward, the deformation decreases everywhere by 15%–30%, likely because the strain efficiently localizes in the orogen and the foreland (Figure 6n). Models S5c and S5d (Figures 6n and 6o) show that a deformation intensity similar to the reference model can be reached if the total convergence velocity is applied to either the lower or the upper plates. Overall, a fast convergence rate controls the intensity of the deformation and its localization. In these models, the contribution of the subducting plate velocity seems more important than that of the overriding plate, although a fast overriding-plate velocity (S5d) can lead to similar degree of deformation as in the reference model. The strain-rate distribution in the overriding plate does not depend on the side of the prescribed velocity. The models that prescribe velocity from the west with the subducting plate (S5c) or from the east with the overriding upper plate (S5d), show similar structures and patterns (Figures 6o and 6p).

3.2.5. Relative Contribution and Importance of Each Factor

By analyzing the maximum deviations in strain localization between the reference model (S1) and the model variants, we can determine the relative importance of each factor in controlling the distribution of strain rates within the overriding plate in Sierras Pampeanas (Figure 7). This study reveals that the strength of continental sediments (S3a–d) and the friction coefficient of the subduction interface (S2a–d) are in the range of the parameters tested, and are most important for localizing deformation at the surface of our models.

The maximum deviation in rate of strain localization at the trench is 994%, which occurs for S2a, indicates that a low friction coefficient at the subduction interface leads to the greatest degree of strain localization at the trench. The deviations decrease as the friction coefficient increases, with S2b, S2c, and S2d showing maximum deviations of −97% or less.

The maximum deviation in rate of strain localization in the flat segment of the overriding plate is 423%, which occurs for S3a, indicating that stronger continental sediments lead to higher strain rate at the trench. The deviations decrease as the strength of continental sediments decreases, with S3d showing a maximum deviation of 157%, the trench accommodates less deformation. Among the models with topography variations (S4), S4c shows the highest maximum deviation of 38%, indicating that the presence of topography related to the orogen likely plays a significant role in transmitting the stress in the flat segment.

The maximum deviation in strain rate in the shallow-slab segment of the overriding plate is −36% for S3c, indicating that weaker continental sediments lead to a higher degree of strain localization in this area. The deviations

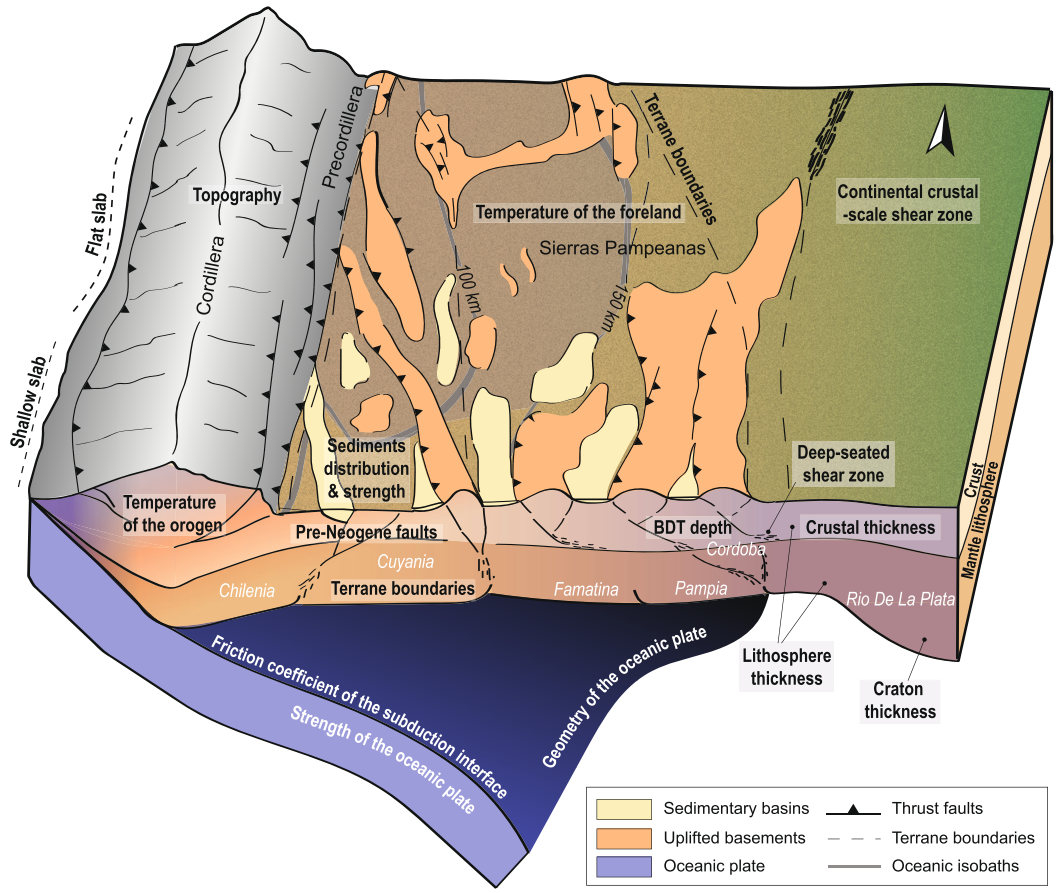


Figure 8. Schematic 3D diagram with relevant forcing factors (in bold) and inherited structures that can affect strain localization and the foreland deformation style in the Sierras Pampeanas.

increase as the strength of continental sediments increases, with S3a showing a maximum deviation of −35%. Among the models with topography variations (S4), S4a shows the greatest maximum deviation of −25%, indicating that in this case topography plays a significant role in localizing deformation in the shallow portion of the Sierras Pampeanas foreland.

4. Discussion

To analyze the roles of inherited heterogeneities in the continental plate and oceanic plate geometry regarding deformation characteristics in the upper plate we assess the relative contribution of overriding plate strength with respect to strain localization along-strike. We first compare the distribution of modeled strain-rate patterns with mapped structures (Section 4.1). Next, we discuss each of the tested key factors and how they affect the stress distribution in our model, and their contribution toward strain localization. In this context, we discuss the role of shallow and deep-seated structures (i.e., sediment strength, topography, and the thermal state and thickness of the lithosphere, Section 4.2, Figure 8). Finally, we examine the effect of slab geometry (flat, shallow, and steep) regarding the distribution and style of deformation in the foreland (Section 4.3).

4.1. Correlation With Mapped Structures

Our modeling results can be compared with mapped surface faults. Although we do not implement faults in the models explicitly, sediment accumulation is partly associated with their activity. In the investigated area, Mesozoic deposits are controlled by normal-fault bounded, extensional basins, while Cenozoic reverse faults

19449194, 2023, 8, Downloaded from https://agupubs.onlinelibrary.wiley.com/doi/10.1029/2023TC007765 by Rwth Aachen Hochschulbibliothe, Wiley Online Library on [15/01/2024]. See the Terms and Conditions (https://onlinelibrary.wiley.com/terms-and-conditions) on Wiley Online Library for rules of use; OA articles are governed by the applicable Creative Commons License

19449194, 2023, 8, Downloaded from https://agupubs.onlinelibrary.wiley.com/doi/10.1029/2023TC007765 by Rwth Aachen Hochschulbibliothe, Wiley Online Library on [15/01/2024]. See the Terms and Conditions (https://onlinelibrary.wiley.com/terms-and-conditions) on Wiley Online Library for rules of use; OA articles are governed by the applicable Creative Commons License

cause sediment accumulation at their footwalls. Therefore, sediment strength and pre-existing faults related to a paleo-tectonic kinematic regime may strongly affect the location of deformation, which explains why structures resulting from the strain-rate pattern of the reference model are spatially well-correlated with exposed faults (Figures 4a and 4b). In particular, the strain-rate distribution in the reference model correlates with Quaternary faults located at the front of the orogen in the thrust belts and uplifted blocks of the foreland (e.g., Malargue FTB, San Rafael Block), at the borders of the basins (e.g., Cuyo Basin), and within intermontane basins bounded by faults uplifting the Sierras Pampeanas basement blocks. In some cases, inherited pre-Andean structures have been reactivated that were associated with the amalgamation of Paleozoic crustal terranes at the western margin of Gondwana (Introcaso & Ruiz, 2001; Ortiz et al., 2021; Vietor & Echtler, 2006). For instance, modeled faults associated with the Desaguadero-Bermejo lineament (29°–32°S) close to the Sierra Valle Fértil in the western Sierras Pampeanas (Figure 4b, Introcaso & Ruiz, 2001) are associated with structures related to the Ordovician collision of the Cuyania and Pampia terranes (Ramos, 2010). This strike-slip fault was reactivated during the Neogene (Introcaso & Ruiz, 2001). The model also predicts the reactivation of the Transbrazilian lineament (TBL), a major Proterozoic transpressive shear zone that borders the thicker mantle lithosphere of the Rio de la Plata craton (Figure 4b, Cordani et al., 2013; Casquet et al., 2018). In contrast, the forearc across all subduction segments is subjected to a low degree of deformation and acts as a rigid body (Hackney et al., 2006; Tassara, 2005; Tassara & Yáñez, 2003), although previous studies have shown that the forearc experienced a certain degree of Quaternary transpressional deformation (González et al., 2003; Melnick et al., 2006; Regard et al., 2010). The previously observed forearc deformation is controlled by the long-term weakening associated with strain partitioning that is caused by oblique plate convergence (Eisermann et al., 2021; Melnick et al., 2006; Rosenau et al., 2006), which is not considered in our model. Other regions that exhibit a low degree of deformation include the foreland above the flat-slab segment (Figure 5a) and the back-arc in the steep-slab segment (Figure 5c). In the latter case, most of the deformation is related to pre-Neogene structures (e.g., Folguera & Zárate, 2009).

4.2. Upper-Plate Control on Strain Localization

The strength of the overriding plate controls strain localization and results from variations in both brittle and viscous strength (Babeyko et al., 2006; Jammes & Huismans, 2012; Liu et al., 2022; Mouthereau et al., 2013). Several processes may weaken the overriding plate and influence the localization of deformation (e.g., Gerbault et al., 2009). In our study we distinguished between shallow and deep-seated contributors, depending on their control on the frictional and viscous strength, respectively.

An important component of the stress is transmitted through the frictional regime (Figure 5), thus shallow contributors can significantly affect strain localization through frictional weakening. The variations in frictional strength are related to the tectonic history of the region and are modulated by several features. These include sediment strength relative to the underlying structures (Babeyko et al., 2006; Erdős et al., 2015; Liu et al., 2022; Mescua et al., 2016), the presence of inherited (pre-Andean) faults and fabrics and their orientation with respect to the convergence direction (Allmendinger et al., 1983; Kley, 1999; Kley & Monaldi, 2002), and topography (Chen & Molnar, 1983; Liu et al., 2022; Mareschal & Jaupart, 2011; Molnar & Tapponnier, 1975; Stüwe, 2007). In turn, the deep-seated contributors are those affecting the thermal state of the crust and the lithospheric mantle, and thus, viscous strength. Spatial variations in viscous strength are influenced by the thickness and composition of the crust and lithospheric mantle, and these characteristics are governed by the geological history of a region (e.g., Alvarado et al., 2007; Gerbault et al., 2002, 2003, 2009; Marot et al., 2014; Rodriguez Piceda, Scheck-Wenderoth, Cacace, et al., 2022). The extent to which shallow and deep-seated contributors interact and affect the strength of the overriding plate in the SCA, is discussed in the following sections and summarized in Figure 9.

4.2.1. Shallow Structures

Previous studies have highlighted the important role of the thickness and strength of sediments in shallow strain localization (Babeyko et al., 2006; Erdős et al., 2015; Liu et al., 2022; Mescua et al., 2016). In the Central Andes (~24°S), the presence of thick, mechanically weak Palaeozoic sediments in the foreland spatially correlates with a southward change of deformational style from thin-skinned to thick-skinned deformation, which marks the transition between the Subandean FTB and the broken foreland province of the Santa Barbara System of northwestern Argentina (Allmendinger et al., 1983; McGroder et al., 2015; Pearson et al., 2013). The results of numerical models addressing the tectonic style in that region have shown that a low friction coefficient of the

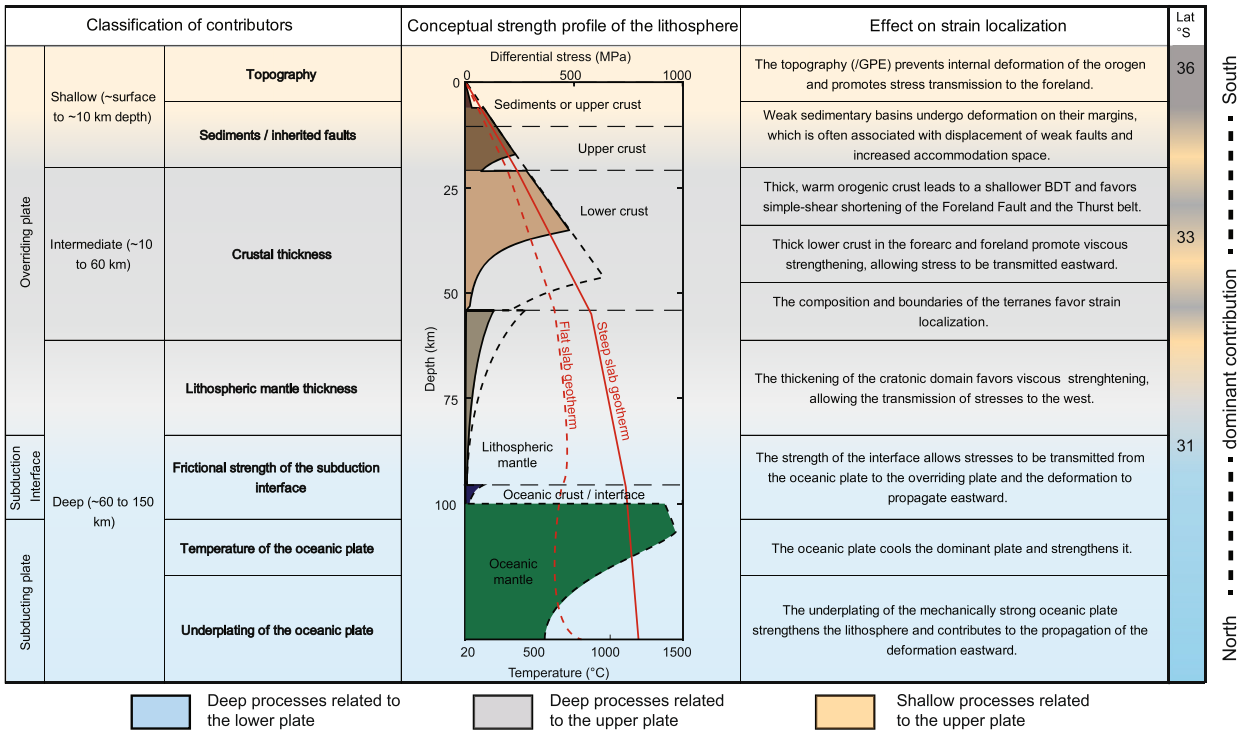


Figure 9. Summary of the main contributors to strain localization in the southern Central Andes indicates a north-south-directed switch from deep to shallow-seated factors.

sediments (<0.05) promotes asymmetric deformation, a simple-shear and thin-skinned deformation style, which may constitute a necessary condition to initiate foreland underthrusting of the Brazilian Shield (Liu et al., 2022; Pons et al., 2022; Sobolev et al., 2006). Additionally, Ibarra et al. (2019) proposed that deformation tends to localize within the areas with large lateral variations of crustal strength, such as the foreland where a thick sedimentary layer is present. In line with these studies, our new results in the southern Central Andes show that the distribution of sediments inherited from past tectonic events largely controls shallow strain localization (Figures 2d, 6–9 and Figures S14a–S14c in Supporting Information S1). Sediments tend to accumulate at the footwall of the faults or close to uplifted basement blocks. In addition, some of these depocenters had already formed during Palaeozoic mountain building and Mesozoic extension, which could also have weakened the basement rocks (Mescua et al., 2016). In our model, efficient simple-shear shortening is favored by the thick sedimentary layer of the foreland basin, which generates a detachment fault connecting areas characterized by plastic (brittle) and viscous strain rates in the upper and lower crust, respectively (Figure 5). This is comparable to the existence of a shear zone at mid to lower crustal levels in the western Principal Cordillera proposed by previous work based on active seismicity (Farías et al., 2010) and numerical modeling (Gerbault et al., 2009). In case that such a connection is not possible, shortening is accommodated by pure shear and deformation distributes along multiple symmetrical faults (Figure 5). Model variations S3a–d show that weaker sediments are required to localize the deformation along specific discrete faults and structures (e.g., at the borders of the uplifted basement blocks; Figure 6 and Figure S14c in Supporting Information S1). Conversely, strong sediments (e.g., Model S3a) with a small strength contrast with respect to the upper crust lead to the formation of a broad, diffuse shear zone in the foreland above the flat-slab segment (Figures 6e–6h).

An additional factor that is proposed to exert major control on strain localization is topography (Figure 9). In the orogen, the gravitational potential energy constitutes an important resistive force to orogenic growth (Chen & Molnar, 1983; Liu et al., 2022; Mareschal & Jaupart, 2011; Molnar & Tapponnier, 1975; Stüwe, 2007). If horizontal forces are not sufficiently strong to overcome gravitational stresses exerted by the growing topography in the orogen, the horizontal stresses migrate laterally to the periphery of the orogen and strain localizes in the foreland. This effect is highlighted in Model S4c (Figure 6k), where no topography is allowed to grow, thus the deformation is less efficiently transmitted and localized in the weak areas of the foreland. Topography can also

19449194, 2023, 8, Downloaded from https://agupubs.onlinelibrary.wiley.com/doi/10.1029/2023TC007765 by Rwth Aachen Hochschulbibliothe, Wiley Online Library on [15/01/2024]. See the Terms and Conditions (https://onlinelibrary.wiley.com/terms-and-conditions) on Wiley Online Library for rules of use; OA articles are governed by the applicable Creative Commons License

19449194, 2023, 8, Downloaded from https://agupubs.onlinelibrary.wiley.com/doi/10.1029/2023TC007765 by Rwth Aachen Hochschulbibliothe, Wiley Online Library on [15/01/2024]. See the Terms and Conditions (https://onlinelibrary.wiley.com/terms-and-conditions) on Wiley Online Library for rules of use; OA articles are governed by the applicable Creative Commons License

exert an indirect effect on the localization of deformation when the bounding faults of the foreland basement blocks and adjacent sediment depocenters are taken into account, which explains the localization of deformation as discussed above. In the alternative models without initial topography (Model S4a, Figure 6i) or where no topography is allowed to grow (Model S4c, Figure 6k), the removal of the orogenic load fosters strain localization in the orogen. Additionally, the models without prescribed velocities (Models S4b, Figures 6j and 6i) indicate that a low portion of the strain rate in the modeled northern part of the orogen could result from a dynamic effect related to flow in the asthenospheric mantle.

4.2.2. Effect of Deep-Seated Inherited Structures

The viscous strength of the continental crust and mantle lithosphere strongly depends on their composition, inherited thickness, and their thermal state because of the strong influence of temperature on viscosity (Anikiev et al., 2020; Burov, 2011; Ibarra et al., 2021; Rodriguez Piceda, Scheck-Wenderoth, Cacace, et al., 2022; Sippel et al., 2017). In the orogen, higher temperatures decrease the depth of the brittle-ductile transition favoring viscous deformation and crustal flow which may facilitate the connection with the plastically deforming foreland sediments, ultimately promoting simple-shear deformation (Figure 9, Liu et al., 2022). Additionally, for an orogenic crust of more than 60 km thickness, simple shear is almost always the preferred mode of foreland deformation (Liu et al., 2022). In contrast, a cold, rigid lithosphere can act as an indenter by transmitting horizontal stresses to its front, localizing the deformation at the transition between strong and weak domains (Figure 9), as shown by previous studies at the Chilean margin (e.g., Gerbault et al., 2009; Ibarra et al., 2021; Rodriguez Piceda, Scheck-Wenderoth, Cacace, et al., 2022).

The lithospheric thermal field in the SCA is the result of the contributions from the compositional and thickness configuration of the lithospheric layers and the basal lithospheric heat flow (Rodriguez Piceda, Scheck-Wenderoth, Bott, et al., 2022; Tassara et al., 2006). The crustal thermal field mainly depends on the volumetric radiogenic heat production of the upper crust, whereas the thermal field of the mantle is strongly perturbed by the cooling effect of the subducting slab, which changes as a function of the slab dip and geometry (Rodriguez Piceda, Scheck-Wenderoth, Bott, et al., 2022). In the northern part of the orogen, the effect of the thick felsic radiogenic crust (Figure 2) overprints the cooling effect of the flat slab (Rodriguez Piceda, Scheck-Wenderoth, Bott, et al., 2022). Therefore, the northern part of the orogen would be expected to deform actively, which contradicts our model results and the lack of observed seismicity in the area (ISC catalog, Rodriguez Piceda, Scheck-Wenderoth, Cacace, et al., 2022; Figure S15 in Supporting Information S1). To explain this apparent contradiction (i.e., no deformation of the upper plate), an additional mechanism must be invoked, which is further discussed in Section 4.3. The lithosphere in the northern foreland is characterized by a thinner radiogenic upper crust (Figure 2) which does not overprint the cooling effect of the flat-slab, thus resulting in a colder and stronger lithosphere. This strengthening allows for an efficient stress transmission from the oceanic plate to the continental plate between western and eastern domains above the flat-slab segment (Figure 9). Additionally, the strong, thick cratonic domain (Figure 2f) promotes an efficient transmission of stresses to the west. Consequently, the deformation localizes at the eastern edge of the broken foreland where the most pronounced lateral gradient of lithospheric strength occurs (Figure 5a and Figure S8 in Supporting Information S1). Finally, the deformation is intensified by the overlying weak sediments.

Other deep-seated lithospheric processes, such as eclogitization of the crust and delamination of the lithospheric mantle, which are not considered in our models, could also weaken the overriding plate and facilitate strain localization (Babeyko et al., 2006; Sobolev et al., 2006). However, in the region of the southern Central Andes analyzed here, there is no evidence of delamination and extensive eclogitization below the western Sierras Pampeanas and the Precordillera (Alvarado et al., 2007, 2009; Ammirati et al., 2013, 2015, 2018; Gilbert et al., 2006; Marot et al., 2014). Thick, warm orogenic crust (>∼45 km) can also be subjected to intracrustal convection and partial melting, further weakening the overriding plate (Babeyko et al., 2006). Nevertheless, these weakening processes are not active in the study area since such thickness values are only attained above the flat-slab segment (Assumpção et al., 2013; Rodriguez Piceda et al., 2021; Tassara et al., 2006). In this region, the low basal heat flow prevents such an effect (Barazangi & Isacks, 1976; Jordan, Isacks, Ramos, & Allmendinger, 1983; Jordan, Isacks, Ramos, & Allmendinger, 1983; Jordan, Isacks, & Ramos, 1983; Ramos & Folguera, 2009).

4.3. Lower-Plate Control on Strain Localization

In the SCA, the role of the flat-slab on the tectonic stress regime and the localization of deformation in the upper plate is a matter of ongoing debate (Folguera et al., 2009; Gutscher, 2018; Gutscher et al., 2000; Horton, 2018;

19449194, 2023, 8, Downloaded from https://agupubs.onlinelibrary.wiley.com/doi/10.1029/2023TC007765 by Rwth Aachen Hochschulbibliothe, Wiley Online Library on [15/01/2024]. See the Terms and Conditions (https://onlinelibrary.wiley.com/terms-and-conditions) on Wiley Online Library for rules of use; OA articles are governed by the applicable Creative Commons License

Jordan, Isacks, Ramos, & Allmendinger, 1983; Jordan, Isacks, Ramos, & Allmendinger, 1983; Jordan, Isacks, & Ramos, 1983; Martinod et al., 2020). Eastward-directed compression in the southern Central Andes is thought to be driven by basal shear stresses related to the underlying flat-slab (Gutscher et al., 2000). Additionally, the passage of the flat-slab weakens the overriding plate mechanically by scraping the continental lithospheric mantle, ("bulldozed mantle-keel" model, Axen et al., 2018; Liu & Currie, 2016; Gutscher, 2018) and thermally by exposing the remaining lithosphere to the warmer asthenosphere (Isacks, 1988). More recent studies, however, have emphasized that the stress regime of the overriding plate is probably more influenced by the velocity difference between the overriding plate and the trench rather than by the subduction angle (Faccenna et al., 2017, 2021; Lallemand et al., 2008). The velocity of trench retreat can be perturbed by a rapid change in the subduction angle, which can be caused by the interaction between the slab and the mantle transition zone (Briaud et al., 2020; Cerpa et al., 2015; Čížková & Bina, 2013; Pons et al., 2022). The absolute motion of the South American plate prescribed in model S1 is considered to be the driving force of the Andean orogeny (Husson et al., 2008; Martinod et al., 2010; Sobolev & Babeyko, 2005); nevertheless, when viewed at shorter geological timescales, model variants such as model S5b–d, illustrate that a similar strain rate as in model S1 can be achieved with a different redistribution of plate velocities while maintaining a similar convergence rate (Figures 6 and 7). This implies that at shorter timescales, the convergence rate is potentially more important than absolute plate velocity.

In our simulations, the subduction angle of the oceanic slab also controls the distribution of strain localization in the upper plate (Figure 9). The flat slab propagates stresses eastward causing shortening to take place in front of the flat slab, as proposed by the "bulldozed mantle-keel" models ("slab bulldozing," Axen et al., 2018; Gutscher, 2018). Strain localization could be favored by inherited crustal-scale structures such as the Transbrazilian lineament in the SCA (see Section 4.2.1). Conversely, the cratonic domain also transmits horizontal stresses westward across the continental plate and amplifies the intensity of deformation (Figure 5). Interestingly, our results predict almost no deformation in the upper plate overlying the flat-slab segment (27°–33°S). This is consistent with limited seismic activity observed in the orogenic domain overlying the flat-slab segment (Figure S14 in Supporting Information S1). In line with previous work (e.g., Gerbault et al., 2009; Martinod et al., 2010; Van Hunen et al., 2002), we suggest that this is the result of upper-plate strengthening at these latitudes due to cooling as discussed above (cf. Section 4.2.2) and caused by an underplating effect of the oceanic slab at the base of the continental lithosphere. The notion that the upper plate is shielded from deformation in the flat-slab segment is also supported by the decrease in shortening in the Precordillera at 30°S at approximately 9 Ma, following the arrival of the Juan Fernandez Ridge at 12 Ma (Allmendinger & Judge, 2014; Bello-González et al., 2018; Yáñez et al., 2001).

The colder subduction interface along the flat-slab segment (Figure 5a) also contributes to an increase in the coupling between the plates, locally reaching reach shear stresses >35 MPa at 45 km depth along the flat-subduction segment (Figure S15 in Supporting Information S1). Moreover, the low temperatures of the subduction interface combined with its low frictional strength could deepen the BDT of this discontinuity to 100 km depth (Figure 5a). The shear stresses at the plate interface decrease southward, which is supported by the increased thickness of the trench-fill sediments south of 33°S (Bangs & Cande, 1997; Völker et al., 2013). A comparison with the average shear stress at the plate interface suggested by Lamb and Davis (2003; Figure S3 in Supporting Information S1) shows that our reference model ($f = 0.015$) may underestimate the shear stress at the flat-slab interface, whereas model S2d ($f = 0.07$) may overestimate it.

In contrast to the flat-slab segment, deformation in the steep-slab segment (36°–40°S) localizes along the front of the orogen (Figures 3a and 4c), which shows that deformation cannot be efficiently propagated to the eastern domain if the oceanic slab is steeply dipping. Furthermore, the transition between the steep and flat-slab geometry requires an intermediary shallow segment (32°–36°S). Above this segment a large crustal shear zone develops in the broken foreland that results from the offset of strain localization between the flat and steep slabs. In such a scenario deformation takes place via multiple faults that bound the basement ranges of the Sierras Pampeanas (31°S, Figure 5d), and the strain localization along these faults is enhanced by the presence of weak sediments (Models S2, Figures 6a–6d). From a dynamic point of view, we suggest that the shallowing of the slab generates crustal contraction prior to slab flattening in response to a large transpressive shear zone in the southern Sierras Pampeanas. Accordingly, deformation could be accommodated by a combination of block rotation and strike-slip deformation at the borders of the uplifted basement blocks. This mechanism, which we informally name "flat-slab conveyor," likely been active in other subduction zones with flat-slab segments, such as in Mexico, where slab flattening and tractional coupling drove Neogene clockwise rotation of the Chiapas

19449194, 2023, 8, Downloaded from https://agupubs.onlinelibrary.wiley.com/doi/10.1029/2023TC007765 by Rwth Aachen Hochschulbibliothe, Wiley Online Library on [15/01/2024]. See the Terms and Conditions (https://onlinelibrary.wiley.com/terms-and-conditions) on Wiley Online Library for rules of use; OA articles are governed by the applicable Creative Commons License

Massif (Molina-Garza et al., 2020) or in the Cretaceous-Eocene Laramide flat slab where large-scale rotations of the Chortis (Honduras) block at the southern termination of the flat slab were identified (Molina-Garza et al., 2019).

5. Conclusions

Using 3D data-driven geodynamic subduction modeling, we analyzed the relative contribution of subducting plate geometry and structural inheritance of the overriding plate on present-day strain localization in the southern Central Andes between 27° and 41°S, which corresponds to the transition between the flat to steep subduction segments in South America. First, the models confirm the results from previous studies showing that the flat slab controls upper-plate deformation in the northern part of the SCA by cooling and further strengthening the overriding plate, protecting the plate from pronounced deformation (Liu et al., 2021; Rodriguez Piceda, Scheck-Wenderoth, Cacace, et al., 2022). Consequently, deformation propagates toward the eastern edge by flat-slab bulldozing (Axen et al., 2018; Gutscher, 2018). A broad, complex shear zone develops with multiple faults at the transition from flat to steep-slab subduction, resembling the thin-skinned to thick-skinned transition seen at these latitudes.

The inherited structures in the overriding plate amplifies strain localization between the flat and steep-slab subduction segments in a multi-faceted way. (a) The distribution of sedimentary rocks can serve as an indicator of major fault distribution, as depocenters tend to form at the footwalls of these faults. Consequently, the presence of shallow, weak inherited faults associated with weak sediments can significantly amplify surface deformation in the foreland. In fact, the intensity of deformation can increase fourfold (˜221%) when these faults are present compared to a situation where sediments are as strong as the upper crust in our models. (b) Surface topography plays a crucial role in strain localization within the orogen by transmitting horizontal stresses toward the foreland. Conversely, when high topography is absent, there is a notable increase in strain localization of over 40%, primarily in the orogen located above the flat slab. However, high topography has a limited influence in the foreland of the transition zone between 31° and 36°S and is not as significant above the steep slab. (c) In the timescales considered in this study, the thickness of the continental crust also plays a significant role in regulating the temperature within the crust, primarily through radiogenic heating. This, in turn, influences the depth of the BDT. When the felsic crust is thicker, the BDT tends to be shallower. The models confirm previous studies showing that a shallow BDT promotes the formation of deep-seated, asymmetric décollements and facilitates simple-shear shortening in fold-and-thrust belts (Babeyko & Sobolev, 2005; Gerbault et al., 2009). On the other hand, a thinner upper continental crust results in a deeper BDT, as observed in the Sierras Pampeanas. This deeper BDT promotes the activity of multiple symmetric faults and facilitates distributed pure-shear shortening. (d) The presence of inherited crustal-scale fault zones, such as the TBL located within the transition to the cratonic domain, may be preferentially reactivated and localize deformation as seen in the north-eastern Sierras Pampeanas (60°–65°W, 27°–31°S).

In our study, we have also compared the effects of using in the models absolute and relative plate motions on the localization of deformation in the upper plate. We show that there is no significant difference between the two approaches at the timescales considered in the models. Whether we consider the absolute motion of the plates or the relative motion between them, the localization of deformation in the upper plate remains similar, suggesting that the choice between absolute plate motion and relative plate motion may not have a substantial impact on the localization of deformation within the upper plate.

Data Availability Statement

The input files to reproduce the results of this paper are available at the following link https://doi.org/10.5880/GFZ.2.5.2023.001 (Pons et al., 2023). Figures in the paper were made with Paraview and Illustrator. The color scales were taken from Crameri (2018) (https://doi.org/10.5281/zenodo.5501399).

Code availability: The ASPECT code is open source (Bangerth et al., 2021). The models were run with the ASPECT version 2.3.0-pre built with the 9.2.0 version of Deal.ii. We have modified the main ASPECT branch to implement new custom plugins necessary for the model set up and the postprocessing, which are described in Pons et al. (2023).

Acknowledgments
This research was funded by the DeutscheForschungsgemeinschaft (DFG) and the Federal State of Brandenburg under the guidance of the International Research Training Group IGK2018 "SuRfAce processes, TEctonics and Georesources: The Andean foreland basin of Argentina" (STRATEGy DFG Grant STR 373/34-1 to M. Strecker). The authors thank the Computational Infrastructure for Geodynamics (geodynamics.org), which is funded by the National Science Foundation under award EAR-0949446 and EAR-1550901, for supporting the development of ASPECT. The computations of this work were supported by the North-German Supercomputing Alliance (HLRN). S. V. Sobolev was funded by the ERC Synergy Grant Project MEET (Monitoring Earth Evolution through Time, Grant 856555). The authors thank the editors L. Jolivet and L. Husson for handling the manuscript, and M. Gerbault and anonymous reviewer for their thoughtful comments. The authors thank C. Kallich for her comments and suggestions on the design of the figures. Open Access funding enabled and organized by Projekt DEAL.

References

Ahumada, E. A., & Costa, C. H. (2009). Antithetic linkage between oblique Quaternary thrusts at the Andean front, Argentine Precordillera. *Journal of South American Earth Sciences*, *28*(3), 207–216. https://doi.org/10.1016/J.JSAMES.2009.03.008

Allmendinger, R. W., & Gubbels, T. (1996). Pure and simple shear plateau uplift, Altiplano-Puna, Argentina and Bolivia. *Tectonophysics*, *259*(1–3 SPEC. ISS.), 1–13. https://doi.org/10.1016/0040-1951(96)00024-8

Allmendinger, R. W., Jordon, T. E., Kay, S. M., & Isacks, B. L. (1997). The evolution of the Altiplano-Puna plateau of the Central Andes. *Annual Review of Earth and Planetary Sciences*, *25*(1), 139–174. https://doi.org/10.1146/annurev.earth.25.1.139

Allmendinger, R. W., & Judge, P. A. (2014). The Argentine Precordillera: A foreland thrust belt proximal to the subducted plate. *Geosphere*, *10*(6), 1203–1218. https://doi.org/10.1130/GES01062.1

Allmendinger, R. W., Ramos, V. A., Jordan, T. E., Palma, M., & Isacks, B. L. (1983). Paleogeography and Andean structural geometry, northwest Argentina. *Tectonics*, *2*(1), 1–16. https://doi.org/10.1029/TC002i001p00001

Alvarado, P., Barrientos, S., Saez, M., Astroza, M., & Beck, S. (2009). Source study and tectonic implications of the historic 1958 Las Melosas crustal earthquake, Chile, compared to earthquake damage. *Physics of the Earth and Planetary Interiors*, *175*(1), 26–36. https://doi.org/10.1016/j.pepi.2008.03.015

Alvarado, P., Beck, S., & Zandt, G. (2007). Crustal structure of the south-central Andes Cordillera and backarc region from regional waveform modeling. *Geophysical Journal International*, *170*(2), 858–875. https://doi.org/10.1111/j.1365-246x.2007.03452.x

Amante, C., & Eakins, B. (2009). ETOPO1 1 arc-minute global relief model: Procedures, data sources and analysis. https://doi.org/10.7289/V5C8276M

Ammirati, J. B., Alvarado, P., & Beck, S. (2015). A lithospheric velocity model for the flat slab region of Argentina from joint inversion of Rayleigh wave phase velocity dispersion and teleseismic receiver functions. *Geophysical Journal International*, *202*(1), 224–241. https://doi.org/10.1093/gji/ggv140

Ammirati, J.-B., Alvarado, P., Perarnau, M., Saez, M., & Monsalvo, G. (2013). Crustal structure of the Central Precordillera of San Juan, Argentina (31°S) using teleseismic receiver functions. *Journal of South American Earth Sciences*, *46*, 100–109. https://doi.org/10.1016/j.jsames.2013.05.007

Ammirati, J.-B., Venerdini, A., Alcacer, J. M., Alvarado, P., Miranda, S., & Gilbert, H. (2018). New insights on regional tectonics and basement composition beneath the eastern Sierras Pampeanas (Argentine Back-Arc region) from seismological and gravity data. *Tectonophysics*, *740–741*, 42–52. https://doi.org/10.1016/j.tecto.2018.05.015

Anikiev, D., Cacace, M., Bott, J., Gomez Dacal, M. L., & Scheck-Wenderoth, M. (2020). Influence of lithosphere rheology on seismicity in an intracontinental rift: The case of the Rhine Graben. *Frontiers in Earth Science*, *8*, 492. https://doi.org/10.3389/feart.2020.592561

Araneda, M., Asch, G., Bataille, K., Bohm, M., Bruhn, C., Giese, P., et al. (2003). A crustal model along 39°S from a seismic refraction profile-ISSA 2000. *Revista Geologica de Chile*, *30*(1), 83–101. https://doi.org/10.4067/S0716-02082003000100006

Assumpção, M., Feng, M., Tassara, A., & Julià, J. (2013). Models of crustal thickness for South America from seismic refraction, receiver functions and surface wave tomography. *Tectonophysics*, *609*, 82–96. https://doi.org/10.1016/J.TECTO.2012.11.014

Axen, G. J., van Wijk, J. W., & Currie, C. A. (2018). Basal continental mantle lithosphere displaced by flat-slab subduction. *Nature Geoscience*, *11*(12), 961–964. Article 12. https://doi.org/10.1038/s41561-018-0263-9

Babeyko, A. Y., & Sobolev, S. V. (2005). Quantifying different modes of the late Cenozoic shortening in the Central Andes. *Geology*, *33*(8), 621–624. https://doi.org/10.1130/G21126.1

Babeyko, A. Y., Sobolev, S. V., Vietor, T., Oncken, O., & Trumbull, R. B. (2006). Numerical study of weakening processes in the Central Andean Back-Arc. In O. Oncken, G. Chong, G. Franz, P. Giese, H.-J. Götze, V. A. Ramos et al. (Eds.), *The Andes: Active subduction orogeny* (pp. 495–512). Springer. https://doi.org/10.1007/978-3-540-48684-8_24

Bangerth, W., Dannberg, J., Fraters, M., Gassmoeller, R., Glerum, A., Heister, T., & Naliboff, J. (2021). ASPECT v2.3.0 (Version 2.3.0) [software]. Zenodo. https://doi.org/10.5281/zenodo.5131909

Bangs, N. L., & Cande, S. C. (1997). Episodic development of a convergent margin inferred from structures and processes along the southern Chile margin. *Tectonics*, *16*(3), 489–503. https://doi.org/10.1029/97TC00494

Barazangi, M., & Isacks, B. L. (1976). Spatial distribution of earthquakes and subduction of the Nazca plate beneath South America. *Geology*, *4*(11), 686–692. https://doi.org/10.1130/0091-7613(1976)4<686:SDOEAS>2.0.CO;2

Barazangi, M., & Isacks, B. L. (1979). Subduction of the Nazca plate beneath Peru: Evidence from spatial distribution of earthquakes. *Geophysical Journal of the Royal Astronomical Society*, *57*(3), 537–555. https://doi.org/10.1111/j.1365-246X.1979.tb06778.x

Barredo, S. P., & Sharkov, E. (2012). Geodynamic and tectonostratigrafic study of a continental rift: The Triassic Cuyana Basin, Argentina. *Tectonics—Recent Advances*, *346*, 99–130.

Barrionuevo, M., Liu, S., Mescua, J., Yagupsky, D., Quinteros, J., Giambiagi, L., et al. (2021). The influence of variations in crustal composition and lithospheric strength on the evolution of deformation processes in the southern Central Andes: Insights from geodynamic models. *International Journal of Earth Sciences*, *110*(7), 2361–2384. https://doi.org/10.1007/s00531-021-01982-5

Becker, T. W., Schaeffer, A. J., Lebedev, S., & Conrad, C. P. (2015). Toward a generalized plate motion reference frame. *Geophysical Research Letters*, *42*(9), 3188–3196. https://doi.org/10.1002/2015GL063695

Bello-González, J. P., Contreras-Reyes, E., & Arriagada, C. (2018). Predicted path for hotspot tracks off South America since Paleocene times: Tectonic implications of ridge-trench collision along the Andean margin. *Gondwana Research*, *64*, 216–234. https://doi.org/10.1016/j.gr.2018.07.008

Bovy, B. (2021). fastscape-lem/fastscape: Release v0.1.0beta3. *Zenodo*. https://doi.org/10.5281/zenodo.4435110

Braun, J., & Willett, S. D. (2013). A very efficient O(n), implicit and parallel method to solve the stream power equation governing fluvial incision and landscape evolution. *Geomorphology*, *180–181*, 170–179. https://doi.org/10.1016/j.geomorph.2012.10.008

Briaud, A., Agrusta, R., Faccenna, C., Funiciello, F., & van Hunen, J. (2020). Topographic fingerprint of deep mantle subduction. *Journal of Geophysical Research: Solid Earth*, *125*(1), e2019JB017962. https://doi.org/10.1029/2019JB017962

Brocher, T. (2005). Empirical relations between elastic waves peeds and density in the Earth's crust. *Bulletin of the Seismological Society of America*, *95*(6), 2081–2092. https://doi.org/10.1785/0120050077

Broens, S., & Pereira, D. M. (2005). Evolución estructural de la zona de transición entre las fajas plegadas y corridas de Aconcagua y Malargüe Provincia de Mendoza. *Revista de la Asociación Geológica Argentina*, *60*(4), 685–695.

Burchfiel, B. C. (1980). Plate tectonics and the continents: A review. In *Studies in geophysics: Continental tectonics* (pp. 15–25). National Academy of Sciences.

Burov, E. (2011). Rheology and strength of the lithosphere. *Marine and Petroleum Geology*, *28*(8), 1402–1443. https://doi.org/10.1016/j.marpetgeo.2011.05.008

19449194, 2023, 8, Downloaded from https://agupubs.onlinelibrary.wiley.com/doi/10.1029/2023TC007765 by Rwth Aachen Hochschulbibliothe, Wiley Online Library on [15/01/2024]. See the Terms and Conditions (https://onlinelibrary.wiley.com/terms-and-conditions) on Wiley Online Library for rules of use; OA articles are governed by the applicable Creative Commons License

Casquet, C., Dahlquist, J. A., Verdecchia, S. O., Baldo, E. G., Galindo, C., Rapela, C. W., et al. (2018). Review of the Cambrian Pampean orogeny of Argentina; a displaced orogen formerly attached to the Saldania Belt of South Africa? *Earth-Science Reviews*, *177*, 209–225. https://doi.org/10.1016/j.earscirev.2017.11.013

Cerpa, N. G., Araya, R., Gerbault, M., & Hassani, R. (2015). Relationship between slab dip and topography segmentation in an oblique subduction zone: Insights from numerical modeling. *Geophysical Research Letters*, *42*(14), 5786–5795. https://doi.org/10.1002/2015GL064047

Chen, W.-P., & Molnar, P. (1983). Focal depths of intracontinental and intraplate earthquakes and their implications for the thermal and mechanical properties of the lithosphere. *Journal of Geophysical Research*, *88*(B5), 4183–4214. https://doi.org/10.1029/JB088iB05p04183

Christensen, N. I., & Mooney, W. D. (1995). Seismic velocity structure and composition of the continental crust: A global view. *Journal of Geophysical Research*, *100*(B6), 9761–9788. https://doi.org/10.1029/95JB00259

Čížková, H., & Bina, C. R. (2013). Effects of mantle and subduction-interface rheologies on slab stagnation and trench rollback. *Earth and Planetary Science Letters*, *379*, 95–103. https://doi.org/10.1016/j.epsl.2013.08.011

Contreras-Reyes, E., Grevemeyer, I., Flueh, E. R., & Reichert, C. (2008). Upper lithospheric structure of the subduction zone offshore of southern Arauco peninsula, Chile, at ∼38°S. *Journal of Geophysical Research*, *113*(B7), B07303. https://doi.org/10.1029/2007JB005569

Cordani, U., Pimentel, M., Ganade, C., & Fuck, R. (2013). The significance of the Transbrasiliano-Kandi tectonic corridor for the amalgamation of West Gondwana. *Brazilian Journal of Genetics*, *43*(3), 583–597. https://doi.org/10.5327/Z2317-48892013000300012

Costa, C., Alvarado, A., Audemard, F., Audin, L., Benavente, C., Bezerra, F. H., et al. (2020). Hazardous faults of South America; compilation and overview. *Journal of South American Earth Sciences*, *104*, 102837. https://doi.org/10.1016/j.jsames.2020.102837

Crameri, F. (2018). Scientific colour maps. Zenodo. http://doi.org/10.5281/zenodo.1243862

Cristallini, E. O., & Ramos, V. A. (2000). Thick-skinned and thin-skinned thrusting in the La Ramada fold and thrust belt. *Tectonophysics*, *317*(3–4), 205–235. https://doi.org/10.1016/s0040-1951(99)00276-0

Dahlen, F. A. (1990). Critical taper model of foldfold-and-thrust belts and accretionary wedges. *Annual Review of Earth and Planetary Sciences*, *18*(1), 55–99. https://doi.org/10.1146/annurev.ea.18.050190.000415

Dai, L., Wang, L., Lou, D., Li, Z.-H., Dong, H., Ma, F., et al. (2020). Slab rollback versus delamination: Contrasting fates of flat-slab subduction and implications for South China evolution in the mesozoic. *Journal of Geophysical Research: Solid Earth*, *125*(4), e2019JB019164. https://doi.org/10.1029/2019JB019164

Dickinson, W. R., & Snyder, W. S. (1978). Plate tectonics of the Laramide orogeny. *Memoirs - Geological Society of America*, *151*, 355–366. https://doi.org/10.1130/MEM151-P355

Eisermann, J. O., Göllner, P. L., & Riller, U. (2021). Orogen-scale transpression accounts for GPS velocities and kinematic partitioning in the Southern Andes. *Communications Earth & Environment*, *2*(1), 167. https://doi.org/10.1038/s43247-021-00241-4

Erdős, Z., Huismans, R. S., & van der Beek, P. (2015). First-order control of syntectonic sedimentation on crustal-scale structure of mountain belts. *Journal of Geophysical Research: Solid Earth*, *120*(7), 5362–5377. https://doi.org/10.1002/2014JB011785

Espurt, N., Funiciello, F., Martinod, J., Guillaume, B., Regard, V., Faccenna, C., & Brusset, S. (2008). Flat subduction dynamics and deformation of the South American plate: Insights from analog modeling. *Tectonics*, *27*(3). https://doi.org/10.1029/2007TC002175

Faccenna, C., Becker, T. W., Holt, A. F., & Brun, J. P. (2021). Mountain building, mantle convection, and supercontinents: Holmes (1931) revisited. *Earth and Planetary Science Letters*, *564*, 116905. https://doi.org/10.1016/j.epsl.2021.116905

Faccenna, C., Oncken, O., Holt, A. F., & Becker, T. W. (2017). Initiation of the Andean orogeny by lower mantle subduction. *Earth and Planetary Science Letters*, *463*, 189–201. https://doi.org/10.1016/J.EPSL.2017.01.041

Fairhead, J. D., & Maus, S. (2003). CHAMP satellite and terrestrial magnetic data help define the tectonic model for South America and resolve the lingering problem of the pre-break-up fit of the South Atlantic Ocean. *The Leading Edge*, *22*(8), 779–783. https://doi.org/10.1190/1.1605081

Farías, M., Comte, D., Charrier, R., Martinod, J., David, C., Tassara, A., et al. (2010). Crustal-scale structural architecture in central Chile based on seismicity and surface geology: Implications for Andean mountain building. *Tectonics*, *29*(3). https://doi.org/10.1029/2009TC002480

Fennell, L. M., Iannelli, S. B., Encinas, A., Naipauer, M., Valencia, V., & Folguera, A. (2019). Alternating contraction and extension in the Southern Central Andes (35°–37°S). *American Journal of Science*, *319*(5), 381–429. https://doi.org/10.2475/05.2019.02

Folguera, A., Naranjo, J. A., Orihashi, Y., Sumino, H., Nagao, K., Polanco, E., & Ramos, V. A. (2009). Retroarc volcanism in the northern San Rafael Block (34°-35°30′S), southern Central Andes: Occurrence, age, and tectonic setting. *Journal of Volcanology and Geothermal Research*, *186*(3–4), 169–185. https://doi.org/10.1016/J.JVOLGEORES.2009.06.012

Folguera, A., & Zárate, M. (2009). La sedimentación neógena continental en el sectorextrandino de Argentina central. *Revista de la Asociación Geológica Argentina*, *64*(4), 692–712.

Folguera, A., & Zárate, M. (2011). *Neogene sedimentation in the Argentine foreland between 34 30'S and 41 S and its relation to the Andes evolution. Cenozoic geology of the Central Andes of Argentina* (pp. 123–134). SCS Publisher.

Franzese, J., Spalletti, L., Pérez, I. G., & Macdonald, D. (2003). Tectonic and paleoenvironmental evolution of Mesozoic sedimentary basins along the Andean foothills of Argentina (32–54 S). *Journal of South American Earth Sciences*, *16*(1), 81–90. https://doi.org/10.1016/s0895-9811(03)00020-8

Fraters, M. (2015). Thermo-mechanically coupled subduction modeling with ASPECT Master's thesis by Menno Fraters. April. https://doi.org/10.13140/RG.2.1.1061.0720

Fuentes, B. H., Starck, D., & Boll, A. (2016). Structure and tectonic evolution of hybrid thick- and thin-skinned systems in the Malargüe fold-thrust belt, Neuquén basin, Argentina. *Geological Magazine*, *153*(5–6), 1066–1084. https://doi.org/10.1017/s0016756816000583

Gans, C. R., Beck, S. L., Zandt, G., Gilbert, H., Alvarado, P., Anderson, M., & Linkimer, L. (2011). Continental and oceanic crustal structure of the Pampean flat slab region, western Argentina, using receiver function analysis: New high-resolution results. *Geophysical Journal International*, *186*(1), 45–58. https://doi.org/10.1111/J.1365-246X.2011.05023.X

Gao, Y., Yuan, X., Heit, B., Tilmann, F., van Herwaarden, D.-P., Thrastarson, S., et al. (2021). Impact of the Juan Fernandez Ridge on the Pampean flat subduction inferred from full waveform inversion. *Geophysical Research Letters*, *48*(21), e2021GL095509. https://doi.org/10.1029/2021GL095509

García, H. P. (2001). Basement-cored uplift deformation in the northern Sierras Pampeanas: Three-dimensional uplift structure, basement deformation, and regional analysis. https://repository.arizona.edu/handle/10150/280775

Gerbault, M., Cembrano, J., Mpodozis, C., Farias, M., & Pardo, M. (2009). Continental margin deformation along the Andean subduction zone: Thermo-mechanical models. *Physics of the Earth and Planetary Interiors*, *177*(3), 180–205. https://doi.org/10.1016/j.pepi.2009.09.001

Gerbault, M., Davey, F., & Henrys, S. (2002). Three-dimensional lateral crustal thickening in continental oblique collision: An example from the Southern Alps, New Zealand. *Geophysical Journal International*, *150*(3), 770–779. https://doi.org/10.1046/j.1365-246X.2002.01737.x

Gerbault, M., Henrys, S., & Davey, F. (2003). Numerical models of lithospheric deformation forming the Southern Alps of New Zealand. *Journal of Geophysical Research*, *108*(B7). https://doi.org/10.1029/2001JB001716

19449194, 2023, 8, Downloaded from https://agupubs.onlinelibrary.wiley.com/doi/10.1029/2023TC007765 by Rwth Aachen Hochschulbibliothe, Wiley Online Library on [15/01/2024]. See the Terms and Conditions (https://onlinelibrary.wiley.com/terms-and-conditions) on Wiley Online Library for rules of use; OA articles are governed by the applicable Creative Commons License

Gerya, T. V., Fossati, D., Cantieni, C., & Seward, D. (2009). Dynamic effects of aseismic ridge subduction: Numerical modeling. *European Journal of Mineralogy*, *21*(3), 649–661. https://doi.org/10.1127/0935-1221/2009/0021-1931

Giambiagi, L., Mescua, J., Bechis, F., Martínez, A., & Folguera, A. (2011). Pre-Andean deformation of the Precordillera southern sector, southern Central Andes. *Geosphere*, *7*(1), 219–239. https://doi.org/10.1130/GES00572.1

Giambiagi, L., Mescua, J., Bechis, F., Tassara, A., & Hoke, G. (2012). Thrust belts of the southern Central Andes: Along-strike variations in shortening, topography, crustal geometry, and denudation. *GSA Bulletin*, *124*(7–8), 1339–1351. https://doi.org/10.1130/B30609.1

Giambiagi, L., Mescua, J., Heredia, N., Farías, P., García-Sansegundo, J., Fernández, C., et al. (2014). Reactivation of Paleozoic structures during Cenozoic deformation in the Cordón del Plata and Southern Precordillera ranges (Mendoza, Argentina). *Journal of Iberian Geology*, *40*(2). https://doi.org/10.5209/rev_JIGE.2014.v40.n2.45302

Giambiagi, L., Tassara, A., Echaurren, A., Julve, J., Quiroga, R., Barrionuevo, M., et al. (2022). Crustal anatomy and evolution of a subduction-related orogenic system: Insights from the Southern Central Andes (22-35°S). *Earth-Science Reviews*, *232*, 104138. https://doi.org/10.1016/j.earscirev.2022.104138

Giambiagi, L. B., Ramos, V. A., Godoy, E., Alvarez, P. P., & Orts, S. (2003). Cenozoic deformation and tectonic style of the Andes, between 33° and 34° south latitude. *Tectonics*, *22*(4). https://doi.org/10.1029/2001TC001354

Gilbert, H., Beck, S., & Zandt, G. (2006). Lithospheric and upper mantle structure of central Chile and Argentina. *Geophysical Journal International*, *165*(1), 383–398. https://doi.org/10.1111/J.1365-246X.2006.02867.X

Gleason, G. C., & Tullis, J. (1995). A flow law for dislocation creep of quartz aggregates determined with the molten salt cell. *Tectonophysics*, *247*(1–4), 1–23. https://doi.org/10.1016/0040-1951(95)00011-B

Glerum, A., Brune, S., Stamps, D. S., & Strecker, M. R. (2020). Victoria continental microplate dynamics controlled by the lithospheric strength distribution of the East African Rift. *Nature Communications*, *11*(1), 2881. https://doi.org/10.1038/S41467-020-16176-X

Glerum, A., Thieulot, C., Fraters, M., Blom, C., & Spakman, W. (2018). Nonlinear viscoplasticity in ASPECT: Benchmarking and applications to subduction. *Solid Earth*, *9*(2), 267–294. https://doi.org/10.5194/SE-9-267-2018

Glerum, A. C., Spakman, W., van Hinsbergen, D. J. J., Thieulot, C., & Pranger, C. (2021). Sensitivity of horizontal surface deformation to mantle dynamics from 3D instantaneous dynamics modeling of the eastern Mediterranean region. Retrieved from https://eartharxiv.org/repository/view/2882/

Global GIS: volcanoes of the world; volcano basic data. (2003). [Shapefile]. American Geological Institute. Retrieved from https://earthworks.stanford.edu/catalog/harvard-glb-volc

Goetze, C., & Evans, B. (1979). Stress and temperature in the bending lithosphere as constrained by experimental rock mechanics. *Geophysical Journal of the Royal Astronomical Society*, *59*(3), 463–478. https://doi.org/10.1111/J.1365-246X.1979.TB02567.X

González, G., Cembrano, J., Carrizo, D., Macci, A., & Schneider, H. (2003). The link between forearc tectonics and Pliocene–Quaternary deformation of the Coastal Cordillera, northern Chile. *Journal of South American Earth Sciences*, *16*(5), 321–342. https://doi.org/10.1016/S0895-9811(03)00100-7

Gutscher, M.-A. (2018). Scraped by flat-slab subduction. *Nature Geoscience*, *11*(12), 889–890. https://doi.org/10.1038/s41561-018-0264-8

Gutscher, M. A., Spakman, W., Bijwaard, H., & Engdahl, E. R. (2000). Geodynamics of flat subduction: Seismicity and tomographic constraints from the Andean margin. *Tectonics*, *19*(5), 814–833. https://doi.org/10.1029/1999TC001152

Hackney, R. I., Echtler, H. P., Franz, G., Götze, H.-J., Lucassen, F., Marchenko, D., et al. (2006). The segmented overriding plate and coupling at the South-Central Chilean Margin (36–42°S). In O. Oncken, G. Chong, G. Franz, P. Giese, H.-J. Götze, V. A. Ramos et al. (Eds.), *The Andes* (pp. 355–374). Springer Berlin Heidelberg. https://doi.org/10.1007/978-3-540-48684-8_17

Haines, P. W., Hand, M., & Sandiford, M. (2001). Palaeozoic synorogenic sedimentation in central and northern Australia: A review of distribution and timing with implications for the evolution of intracontinental orogens. *Australian Journal of Earth Sciences*, *48*(6), 911–928. https://doi.org/10.1046/j.1440-0952.2001.00909.x

Hamza, V. M., & Vieira, F. P. (2012). Global distribution of the lithosphere-asthenosphere boundary: A new look. *Solid Earth*, *3*(2), 199–212. https://doi.org/10.5194/se-3-199-2012

Hayes, G. P., Moore, G. L., Portner, D. E., Hearne, M., Flamme, H., Furtney, M., & Smoczyk, G. M. (2018). Slab2, a comprehensive subduction zone geometry model. *Science*, *362*(6410), 58–61. https://doi.org/10.1126/science.aat4723

Heister, T., Dannberg, J., Gassmöller, R., & Bangerth, W. (2017). High accuracy mantle convection simulation through modern numerical methods–II: Realistic models and problems. *Geophysical Journal International*, *210*(2), 833–851. https://doi.org/10.1093/gji/ggx195

Heredia, N., García-Sansegundo, J., Gallastegui, G., Farias, P., Giacosa, R., Alonso, J. L., et al. (2016). Evolución Geodinámica de los Andes argentino-chilenos y la Península Antártica durante el Neoproterozoico tardío y el Paleozoico Late Neoproterozoic-Paleozoic geodynamic evolution of the Argentine-Chilean Andes and the Antarctic Peninsula. *Trabajos de Geología*, *36*, 237. Article 36. https://doi.org/10.17811/tdg.36.2016.237-278

Hirth, G., & Kohlstedt, D. (2004). Rheology of the upper mantle and the mantle wedge: A view from the experimentalists. *Geophysical Monograph Series*, *138*, 83–105. https://doi.org/10.1029/138GM06

Hirth, G., & Kohlstedt, D. L. (2003). Rheology of the upper mantle and the mantle wedge: A view from the experimentalists upper mantle. We first analyze experimental data to provide a critical review of flow. *Geophysical Monograph Series*, *138*, 83–105. https://doi.org/10.1029/138GM06

Horton, B. (2018). Tectonic regimes of the Central and Southern Andes: Responses to variations in plate coupling during subduction. *Tectonics*, *37*(2), 402–429. https://doi.org/10.1002/2017tc004624

Horton, B. K., Capaldi, T. N., Mackaman-Lofland, C., Perez, N. D., Bush, M. A., Fuentes, F., & Constenius, K. N. (2022). Broken foreland basins and the influence of subduction dynamics, tectonic inheritance, and mechanical triggers. *Earth-Science Reviews*, *234*, 104193. https://doi.org/10.1016/j.earscirev.2022.104193

Horton, B. K., Fuentes, F., Boll, A., Starck, D., Ramirez, S. G., & Stockli, D. F. (2016). Andean stratigraphic record of the transition from backarc extension to orogenic shortening: A case study from the northern Neuquén Basin, Argentina. *Journal of South American Earth Sciences*, *71*, 17–40. https://doi.org/10.1016/j.jsames.2016.06.003

Husson, L., Conrad, C. P., & Faccenna, C. (2008). Tethyan closure, Andean orogeny, and westward drift of the Pacific Basin. *Earth and Planetary Science Letters*, *271*(1–4), 303–310. https://doi.org/10.1016/j.epsl.2008.04.022

Ibarra, F., Liu, S., Meeßen, C., Prezzi, C. B., Bott, J., Scheck-Wenderoth, M., et al. (2019). 3D data-derived lithospheric structure of the Central Andes and its implications for deformation: Insights from gravity and geodynamic modeling. *Tectonophysics*, *766*, 453–468. https://doi.org/10.1016/j.tecto.2019.06.025

Ibarra, F., Meeßen, C., Liu, S., Prezzi, C., & Sippel, J. (2018). Density structure and rheology of northern Argentina: From the Central Andes to the foreland basin. *20*(April), 16756.

19449194, 2023, 8, Downloaded from https://agupubs.onlinelibrary.wiley.com/doi/10.1029/2023TC007765 by Rwth Aachen Hochschulbibliothe, Wiley Online Library on [15/01/2024]. See the Terms and Conditions (https://onlinelibrary.wiley.com/terms-and-conditions) on Wiley Online Library for rules of use; OA articles are governed by the applicable Creative Commons License

Ibarra, F., Prezzi, C. B., Bott, J., Scheck-Wenderoth, M., & Strecker, M. R. (2021). Distribution of temperature and strength in the Central Andean lithosphere and its relationship to seismicity and active deformation. *Journal of Geophysical Research: Solid Earth*, *126*(5). https://doi.org/10.1029/2020JB021231

Introcaso, A., & Ruiz, F. (2001). Geophysical indicators of Neogene strike-slip faulting in the Desaguadero–Bermejo tectonic lineament (northwestern Argentina). *Journal of South American Earth Sciences*, *14*(7), 655–663. https://doi.org/10.1016/S0895-9811(01)00057-8

Isacks, B. (1988). Uplift of the Central Andean Plateau and bending of the Bolivian Orocline. *Journal of Geophysical Research*, *93*(B4), 3211. https://doi.org/10.1029/jb093ib04p03211

Isacks, B. L., & Barazangi, M. (1977). Geometry of Benioff zones. In *Island Arcs, Deep Sea Trenches and Back-Arc Basins* (pp. 99–114). American Geophysical Union (AGU). https://doi.org/10.1029/ME001p0099

Jammes, S., & Huismans, R. S. (2012). Structural styles of mountain building: Controls of lithospheric rheologic stratification and extensional inheritance. *Journal of Geophysical Research*, *117*(B10). https://doi.org/10.1029/2012JB009376

Jensen, E. (2018). Efectos de fluidos hidrotermales en el desarrollo de fallas: Petrografía y propiedades mecánicas [PhD Dissertation, Universidad Católica del Norte]. https://doi.org/10.13140/RG.2.2.34341.35049

Jordan, T. E., & Allmendinger, R. W. (1986). The Sierras Pampeanas of Argentina: A modern analogue of Rocky Mountain foreland deformation. *American Journal of Science*, *286*(10), 737–764. https://doi.org/10.2475/AJS.286.10.737

Jordan, T. E., Isacks, B. L., Allmendinger, R. W., Brewer, J. A., Ramos, V. A., & Ando, C. J. (1983a). Andean tectonics related to geometry of subducted Nazca plate. *Geological Society of America Bulletin*, *94*(3), 341–361. https://doi.org/10.1130/0016-7606(1983)94<341:atrtgo>2.0.co;2

Jordan, T. E., Isacks, B. L., Ramos, V. A., & Allmendinger, R. W. (1983b). Mountain building in the central Andes. *Episodes*, *1983*(3), 20–26. https://doi.org/10.18814/EPIIUGS/1983/V6I3/005

Jordan, T. E., Ramos, V. A., Allmendinger, R. W., & Isacks, B. L. (1984). Andean tectonics related to geometry of subducted Nazca plate: Discussion and reply: Reply. July, 877-880. https://doi.org/10.1130/0016-7606(1984)95<877

Kay, S. M., & Mpodozis, C. (2002). Magmatism as a probe to the Neogene shallowing of the Nazca plate beneath the modern Chilean flat-slab. *Journal of South American Earth Sciences*, *15*(1), 39–57. https://doi.org/10.1016/S0895-9811(02)00005-6

Kley, J. (1999). Geologic and geometric constraints on a kinematic model of the Bolivian orocline. *Journal of South American Earth Sciences*, *12*(2), 221–235. https://doi.org/10.1016/S0895-9811(99)00015-2

Kley, J., & Monaldi, C. R. (1998). Tectonic shortening and crustal thickness in the Central Andes: How good is the correlation-? *Geology*, *26*(8), 723–726. https://doi.org/10.1130/0091-7613(1998)026<0723:TSACTI>2.3.CO;2

Kley, J., & Monaldi, C. R. (2002). Tectonic inversion in the Santa Barbara System of the central Andean foreland thrust belt, northwestern Argentina. *Tectonics*, *21*(6), 11-1–11-18. https://doi.org/10.1029/2002TC902003

Kronbichler, M., Heister, T., & Bangerth, W. (2012). High accuracy mantle convection simulation through modern numerical methods. *Geophysical Journal International*, *191*(1), 12–29. https://doi.org/10.1111/j.1365-246x.2012.05609.x

Lacombe, O., & Bellahsen, N. (2016). Thick-skinned tectonics and basement-involved fold-thrust belts: Insights from selected Cenozoic orogens. *Geological Magazine*, *153*(5–6), 763–810. https://doi.org/10.1017/S0016756816000078

Lallemand, S., Heuret, A., Faccenna, C., & Funiciello, F. (2008). Subduction dynamics as revealed by trench migration. *Tectonics*, *27*(3). https://doi.org/10.1029/2007TC002212

Lamb, S., & Davis, P. (2003). Cenozoic climate change as a possible cause for the rise of the Andes. *Nature*, *425*(6960), 792–797. https://doi.org/10.1038/NATURE02049

Litvak, V. D., Poma, S., Jones, R. E., Fernández Paz, L., Iannelli, S. B., Spagnuolo, M., et al. (2018). The Late Paleogene to Neogene volcanic arc in the Southern Central Andes (28°–37° S). In A. Folguera, E. Contreras-Reyes, N. Heredia, A. Encinas, S. B. Iannelli, V. Oliveros et al. (Eds.), *The evolution of the Chilean-Argentinean Andes* (pp. 503–536). Springer International Publishing. https://doi.org/10.1007/978-3-319-67774-3_20

Liu, S., & Currie, C. A. (2016). Farallon plate dynamics prior to the Laramide orogeny: Numerical models of flat subduction. *Tectonophysics*, *666*, 33–47. https://doi.org/10.1016/J.TECTO.2015.10.010

Liu, S., Sobolev, S. V., Babeyko, A. Y., & Pons, M. (2022). Controls of the foreland deformation pattern in the orogen-foreland shortening system: Constraints from high-resolution geodynamic models. *Tectonics*, *41*(2). https://doi.org/10.1029/2021TC007121

Liu, X., Currie, C. A., & Wagner, L. S. (2021). Cooling of the continental plate during flat-slab subduction. *Geosphere*, *18*(1), 49–68. https://doi.org/10.1130/GES02402.1

Lossada, A., Giambiagi, L., Hoke, G., Au, & Suriano, J. (2017). *Cenozoic uplift and exhumation of the frontal Cordillera between 30° and 35°S and the influence of the subduction dynamics in the flat slab subduction context*. South Central Andes. https://doi.org/10.1007/978-3-319-67774-3_16

Mackwell, S. J., Zimmerman, M. E., & Kohlstedt, D. L. (1998). High-temperature deformation of dry diabase with application to tectonics on Venus. *Journal of Geophysical Research*, *103*(1), 975–984. https://doi.org/10.1029/97JB02671

Manceda, R., & Figueroa, D. (1995). Inversion of the Mesozoic Neuquén rift in the Malargüe fold and thrust belt, Mendoza, Argentina.

Manea, V., & Gurnis, M. (2007). Subduction zone evolution and low viscosity wedges and channels. *Earth and Planetary Science Letters*, *264*(1–2), 22–45. https://doi.org/10.1016/j.epsl.2007.08.030

Mareschal, J.-C., & Jaupart, C. (2011). Energy budget of the Earth. In H. K. Gupta (Ed.), (Éd.), *Encyclopedia of Solid Earth geophysics* (pp. 285–291). Springer Netherlands. https://doi.org/10.1007/978-90-481-8702-7_64

Marot, M., Monfret, T., Gerbault, M., Nolet, G., Ranalli, G., & Pardo, M. (2014). Flat versus normal subduction zones: A comparison based on 3-D regional traveltime tomography and petrological modeling of central Chile and western Argentina (29°–35°S). *Geophysical Journal International*, *199*(3), 1633–1654. https://doi.org/10.1093/gji/ggu355

Martínez, F., Parra, M., Arriagada, C., Mora, A., Bascuñan, S., & Peña, M. (2017). Late Cretaceous to Cenozoic deformation and exhumation of the Chilean Frontal Cordillera (28°–29°S), Central Andes. *Journal of Geodynamics*, *111*, 31–42. https://doi.org/10.1016/j.jog.2017.08.004

Martino, R., Guereschi, A., & Montero, A. (2016). Reactivation, inversion and basement faulting and thrusting in the Sierras Pampeanas of Córdoba (Argentina) during Andean flat-slab deformation. *Geological Magazine*, *1*, 1–30. https://doi.org/10.1017/S0016756816000339

Martinod, J., Gérault, M., Husson, L., & Regard, V. (2020). Widening of the Andes: An interplay between subduction dynamics and crustal wedge tectonics. *Earth-Science Reviews*, *204*, 103170. https://doi.org/10.1016/j.earscirev.2020.103170

Martinod, J., Husson, L., Roperch, P., Guillaume, B., & Espurt, N. (2010). Horizontal subduction zones, convergence velocity and the building of the Andes. *Earth and Planetary Science Letters*, *299*(3–4), 299–309. https://doi.org/10.1016/j.epsl.2010.09.010

McGroder, M. F., Lease, R. O., & Pearson, D. M. (2015). Along-strike variation in structural styles and hydrocarbon occurrences, Subandean fold-and-thrust belt and inner foreland, Colombia to Argentina. *Memoirs - Geological Society of America*, *212*, 79–113. https://doi.org/10.1130/2015.1212(05

19449194, 2023, 8, Downloaded from https://agupubs.onlinelibrary.wiley.com/doi/10.1029/2023TC007765 by Rwth Aachen Hochschulbibliothe, Wiley Online Library on [15/01/2024]. See the Terms and Conditions (https://onlinelibrary.wiley.com/terms-and-conditions) on Wiley Online Library for rules of use; OA articles are governed by the applicable Creative Commons License

Meeßen, C., Sippel, J., Scheck-Wenderoth, M., Heine, C., & Strecker, M. R. (2018). Crustal structure of the Andean Foreland in Northern Argentina: Results from data-integrative three-dimensional density modeling. *Journal of Geophysical Research: Solid Earth*, *123*(2), 1875–1903. https://doi.org/10.1002/2017JB014296

Melnick, D., Charlet, F., Echtler, H. P., & De Batist, M. (2006). Incipient axial collapse of the Main Cordillera and strain partitioning gradient between the central and Patagonian Andes, Lago Laja, Chile. *Tectonics*, *25*(5). https://doi.org/10.1029/2005TC001918

Melnick, D., Maldonado, V., & Contreras, M. (2020). Database of active and potentially-active continental faults in Chile at 1:25,000 scale. *PANGAEA*. https://doi.org/10.1594/PANGAEA.922241

Mescua, J. F., Giambiagi, L., Barrionuevo, M., Tassara, A., Mardonez, D., Mazzitelli, M., & Lossada, A. (2016). Basement composition and basin geometry controls on upper-crustal deformation in the Southern Central Andes (30-36°S). *Geological Magazine*, *153*(5–6), 945–961. https://doi.org/10.1017/S0016756816000364

Mescua, J. F., Giambiagi, L. B., Tassara, A., Gimenez, M., & Ramos, V. A. (2014). Influence of pre-Andean history over Cenozoic foreland deformation: Structural styles in the Malargüe fold-and-thrust belt at 35 S, Andes of Argentina. *Geosphere*, *10*(3), 585–609. https://doi.org/10.1130/GES00939.1

Molina-Garza, R. S., Pindell, J., & Cortés, P. C. M. (2020). Slab flattening and tractional coupling drove Neogene clockwise rotation of Chiapas Massif, Mexico: Paleomagnetism of the Eocene El Bosque Formation. *Journal of South American Earth Sciences*, *104*, 102932. https://doi.org/10.1016/j.jsames.2020.102932

Molina-Garza, R. S., van Hinsbergen, D. J., Boschman, L. M., Rogers, R. D., & Ganerød, M. (2019). Large-scale rotations of the Chortis Block (Honduras) at the southern termination of the Laramide flat slab. *Tectonophysics*, *760*, 36–57. https://doi.org/10.1016/j.tecto.2017.11.026

Molnar, P., & Tapponnier, P. (1975). Cenozoic Tectonics of Asia: Effects of a continental collision. *Science*, *189*(4201), 419–426. https://doi.org/10.1126/science.189.4201.419

Mon, R., & Salfity, J. (1995). Tectonic evolution of the Andes of northern Argentina. In *Petroleum basins of south America* (Vol. 62). AAPG Special Volumes.

Moscoso, R., & Mpodozis, C. (1988). Estilos estructurales en el norte chico de Chile (28-31°S), regiones de Atacama y Coquimbo. *Andean Geology*, *15*(2). Article 2. https://doi.org/10.5027/andgeoV15n2-a04

Mouthereau, F., Watts, A. B., & Burov, E. (2013). Structure of orogenic belts controlled by lithosphere age. *Nature Geoscience*, *6*(9), 785–789. https://doi.org/10.1038/ngeo1902

Mpodozis, C., & Kay, S. M. (1990). Provincias magmáticas ácidas y evolución tectónica de Gondwana: Andes chilenos (28-31 S). *Andean Geology*, *17*(2), 153–180. https://doi.org/10.5027/andgeoV17n2-a03

Muldashev, I. A., & Sobolev, S. V. (2020). What controls maximum magnitudes of giant subduction earthquakes? *Geochemistry, Geophysics, Geosystems*, *21*(9). https://doi.org/10.1029/2020GC009145

Murnaghan, F. D. (1944). The compressibility of media under extreme pressures. *Proceedings of the National Academy of Sciences*, *30*(9), 244–247. https://doi.org/10.1073/pnas.30.9.244

Neuharth, D., Brune, S., Glerum, A. C., Morley, C. K., Yuan, X., & Braun, J. (2021). Flexural strike-slip basins. Retrieved from https://eartharxiv.org/repository/view/2439/

Olivar, J., Nacif, S., Fennell, L., & Folguera, A. (2018). Within plate seismicity analysis in the segment between the high Cordillera and the Precordillera of northern Mendoza (Southern Central Andes). *Geodesy and Geodynamics*, *9*(1), 13–24. https://doi.org/10.1016/j.geog.2017.09.004

Oncken, O., Boutelier, D., Dresen, G., & Schemmann, K. (2012). Strain accumulation controls failure of a plate boundary zone: Linking deformation of the Central Andes and lithosphere mechanics. *Geochemistry, Geophysics, Geosystems*, *13*(12). https://doi.org/10.1029/2012GC004280

Oncken, O., Hindle, D., Kley, J., Elger, K., Victor, P., & Schemmann, K. (2006). Deformation of the Central Andean upper plate system—Facts, fiction, and constraints for plateau models. *The Andes*, *3–27*, 3–27. https://doi.org/10.1007/978-3-540-48684-8_1

Ortiz, G., Stevens Goddard, A. L., Fosdick, J. C., Alvarado, P., Carrapa, B., & Cristofolini, E. (2021). Fault reactivation in the Sierras Pampeanas resolved across Andean extensional and compressional regimes using thermochronologic modeling. *Journal of South American Earth Sciences*, *112*, 103533. https://doi.org/10.1016/j.jsames.2021.103533

Pearson, D. M., Kapp, P., DeCelles, P. G., Reiners, P. W., Gehrels, G. E., Ducea, M. N., & Pullen, A. (2013). Influence of pre-Andean crustal structure on Cenozoic thrust belt kinematics and shortening magnitude: Northwestern Argentina. *Geosphere*, *9*(6), 1766–1782. https://doi.org/10.1130/GES00923.1

Pesicek, J. D., Engdahl, E. R., Thurber, C. H., DeShon, H. R., & Lange, D. (2012). Mantle subducting slab structure in the region of the 2010 M8.8 Maule earthquake (30-40°S), Chile: Mantle subducting slab structure in Chile. *Geophysical Journal International*, *191*(1), 317–324. https://doi.org/10.1111/j.1365-246X.2012.05624.x

Pfiffner, O. A. (2017). Thick-skinned and thin-skinned tectonics: A global perspective. *GeoscienceGlobal Perspectives*, *7*(3), 71. https://doi.org/10.3390/geosciences7030071

Pilger, R. H., Jr. (1981). Plate reconstructions, aseismic ridges, and low-angle subduction beneath the Andes. *GSA Bulletin*, *92*(7), 448–456. https://doi.org/10.1130/0016-7606(1981)92<448:PRARAL>2.0.CO;2

Pons, M., Rodriguez Piceda, C., Sobolev, S., Scheck-Wenderoth, M., & Strecker, M. R. (2023). 3D geodynamic data-driven model of the Southern Central Andes (Version 1) [Dataset]. GFZ Data Services. https://doi.org/10.5880/GFZ.2.5.2023.001

Pons, M., Sobolev, S. V., Liu, S., & Neuharth, D. (2022). Hindered trench migration due to slab steepening controls the formation of the Central Andes. *Journal of Geophysical Research: Solid Earth*, *127*(12), e2022JB025229. https://doi.org/10.1029/2022JB025229

Ramos, V. (2010). The Grenville-age basement of the Andes. *Journal of South American Earth Sciences*, *29*(1), 77–91. https://doi.org/10.1016/j.jsames.2009.09.004

Ramos, V. A., Cristallini, E. O., & Pérez, D. J. (2002). The Pampean flat-slab of the Central Andes. *Journal of South American Earth Sciences*, *15*(1), 59–78. https://doi.org/10.1016/s0895-9811(02)00006-8

Ramos, V. A., & Folguera, A. (2009). Andean flat-slab subduction through time. *Geological Society - Special Publications*, *327*(1), 31–54. https://doi.org/10.1144/SP327.3

Ramos, V. A., & Scientific, N. (2002). Flat-slab subduction in the Andes. *Journal of South American Earth Sciences*, *15*(1), 1–2. https://doi.org/10.1016/s0895-9811(02)00011-1

Ranalli, G. (1997). Rheology and deep tectonics. *Annals of Geophysics*, *40*(3), 3. https://doi.org/10.4401/ag-3893

Regard, V., Saillard, M., Martinod, J., Audin, L., Carretier, S., Pedoja, K., et al. (2010). Renewed uplift of the Central Andes Forearc revealed by coastal evolution during the Quaternary. *Earth and Planetary Science Letters*, *297*(1), 199–210. https://doi.org/10.1016/j.epsl.2010.06.020

Riesner, M., Lacassin, R., Simoes, M., Carrizo, D., & Armijo, R. (2018). Revisiting the crustal structure and kinematics of the Central Andes at 33.5°S: Implications for the mechanics of Andean Mountain Building. *Tectonics*, *37*(5), 1347–1375. https://doi.org/10.1002/2017TC004513

19449194, 2023, 8, Downloaded from https://agupubs.onlinelibrary.wiley.com/doi/10.1029/2023TC007765 by Rwth Aachen Hochschulbibliothe, Wiley Online Library on [15/01/2024]. See the Terms and Conditions (https://onlinelibrary.wiley.com/terms-and-conditions) on Wiley Online Library for rules of use; OA articles are governed by the applicable Creative Commons License

Rodriguez Piceda, C., Scheck-Wenderoth, M., Bott, J., Gomez Dacal, M. L., Cacace, M., Pons, M., et al. (2022). Controls of the lithospheric thermal field of an ocean-continent subduction zone: The southern central Andes. *Lithosphere*, *2022*(1), 2237272. https://doi.org/10.2113/2022/2237272

Rodriguez Piceda, C., Scheck-Wenderoth, M., Cacace, M., Bott, J., & Strecker, M. R. (2022b). Long-term lithospheric strength and upper-plate seismicity in the southern central Andes, 29°–39°S. *Geochemistry, Geophysics, Geosystems*, *23*(3), 22. https://doi.org/10.1029/2021GC010171

Rodriguez Piceda, C., Scheck Wenderoth, M., Gomez Dacal, M. L., Bott, J., Prezzi, C. B., & Strecker, M. R. (2021). Lithospheric density structure of the southern central Andes constrained by 3D data-integrative gravity modeling. *International Journal of Earth Sciences*, *110*(7), 2333–2359. https://doi.org/10.1007/S00531-020-01962-1

Rose, I., Buffett, B., & Heister, T. (2017). Stability and accuracy of free surface time integration in viscous flows. *Physics of the Earth and Planetary Interiors*, *262*, 90–100. https://doi.org/10.1016/J.PEPI.2016.11.007

Rosenau, M., Melnick, D., & Echtler, H. (2006). Kinematic constraints on intra-arc shear and strain partitioning in the southern Andes between 38°S and 42°S latitude. *Tectonics*, *25*(4). https://doi.org/10.1029/2005TC001943

Scarfi, L., & Barbieri, G. (2019). New insights on the tectonic structure of the Southern Central Andes – Western Argentina – From seismic tomography. *Geology, Earth & Marine Sciences*, *1*(1). https://doi.org/10.31038/GEMS.2019113

Schellart, W. P. (2020). Control of subduction zone age and size on flat slab subduction. *Frontiers in Earth Science*, *8*. https://doi.org/10.3389/FEART.2020.00026/TEXT

Schellart, W. P., & Strak, V. (2021). Geodynamic models of short-lived, long-lived and periodic flat slab subduction. *Geophysical Journal International*, *226*(3), 1517–1541. https://doi.org/10.1093/gji/ggab126

Sdrolias, M., & Müller, R. D. (2006). Controls on back-arc basin formation. *Geochemistry, Geophysics, Geosystems*, *7*(4). https://doi.org/10.1029/2005GC001090

Sippel, J., Meeßen, C., Cacace, M., Mechie, J., Fishwick, S., Heine, C., et al. (2017). The Kenya rift revisited: Insights into lithospheric strength through data-driven 3-D gravity and thermal modeling. *Solid Earth*, *8*(1), 45–81. https://doi.org/10.5194/se-8-45-2017

Sobolev, S. V., & Babeyko, A. Y. (1994). Modeling of mineralogical composition, density and elastic wave velocities in anhydrous magmatic rocks. *Surveys in Geophysics*, *15*(5), 515–544. https://doi.org/10.1007/BF00690173

Sobolev, S. V., & Babeyko, A. Y. (2005). What drives orogeny in the Andes? *Geology*, *33*(8), 617–620. https://doi.org/10.1130/G21557.1

Sobolev, S. V., Babeyko, A. Y., Koulakov, I., & Oncken, O. (2006). Mechanism of the Andean Orogeny: Insight from numerical modeling. In *The Andes* (pp. 513–535). Springer Berlin Heidelberg. https://doi.org/10.1007/978-3-540-48684-8_25

Stalder, N. F., Herman, F., Fellin, M. G., Coutand, I., Aguilar, G., Reiners, P. W., & Fox, M. (2020). The relationships between tectonics, climate and exhumation in the Central Andes (18–36°S): Evidence from low-temperature thermochronology. *Earth-Science Reviews*, *210*, 103276. https://doi.org/10.1016/j.earscirev.2020.103276

Stüwe, K. (2007). *Geodynamics of the lithosphere*. Springer-Verlag Berlin Heidelberg.

Tassara, A. (2005). Interaction between the Nazca and South American plates and formation of the Altiplano–Puna plateau: Review of a flexural analysis along the Andean margin (15°–34°S). *Andean Geodynamics*, *399*(1), 39–57. https://doi.org/10.1016/j.tecto.2004.12.014

Tassara, A., & Echaurren, A. (2012). Anatomy of the Andean subduction zone: Three-dimensional density model upgraded and compared against global-scale models. *Geophysical Journal International*, *189*(1), 161–168. https://doi.org/10.1111/j.1365-246X.2012.05397.x

Tassara, A., Götze, H.-J., Schmidt, S., & Hackney, R. (2006). Three-dimensional density model of the Nazca plate and the Andean continental margin. *Journal of Geophysical Research*, *111*(B9), B09404. https://doi.org/10.1029/2005JB003976

Tassara, A., & Yáñez, G. (2003). Relación entre el espesor elástico de la litosfera y la segmentación tectónica del margen andino (15-47°S). *Revista Geologica de Chile*, *30*(2), 159–186. https://doi.org/10.4067/S0716-02082003000200002

Uliana, M. A., Arteaga, M. E., Legarreta, L., Cerdán, J. J., & Peroni, G. O. (1995). Inversion structures and hydrocarbon occurrence in Argentina. *Geological Society, London, Special Publications*, *88*(1), 211–233. https://doi.org/10.1144/GSL.SP.1995.088.01.13

Uliana, M. A., Biddle, K. T., & Cerdan, J. (1989). Mesozoic extension and the formation of Argentine sedimentary basins. chapter 39: analogs.

Van Hunen, J., Van Den Berg, A. P., & Vlaar, N. J. (2002). On the role of subducting oceanic plateaus in the development of shallow flat subduction. *Tectonophysics*, *352*(3–4), 317–333. https://doi.org/10.1016/S0040-1951(02)00263-9

Van Keken, P. E., Wada, I., Sime, N., & Abers, G. A. (2019). Thermal structure of the forearc in subduction zones: A comparison of methodologies. *Geochemistry, Geophysics, Geosystems*, *20*(7), 3268–3288. https://doi.org/10.1029/2019GC008334

Vietor, T., & Echtler, H. (2006). Episodic Neogene southward growth of the Andean subduction orogen between 30°S and 40°S—Plate motions, mantle flow, climate, and upper-plate structure. In O. Oncken, G. Chong, G. Franz, P. Giese, H.-J. Götze, V. A. Ramos et al. (Eds.), *The Andes* (pp. 375–400). Springer Berlin Heidelberg. https://doi.org/10.1007/978-3-540-48684-8_18

Völker, D., Geersen, J., Contreras-Reyes, E., & Reichert, C. (2013). Sedimentary fill of the Chile Trench (32–46°S): Volumetric distribution and causal factors. *Journal of the Geological Society*, *170*(5), 723–736. https://doi.org/10.1144/jgs2012-119

Wada, I., & Wang, K. (2009). Common depth of slab-mantle decoupling: Reconciling diversity and uniformity of subduction zones. *Geochemistry, Geophysics, Geosystems*, *10*(10). https://doi.org/10.1029/2009GC002570

Wagner, L. S., Beck, S., & Zandt, G. (2005). Upper mantle structure in the south central Chilean subduction zone (30° to 36°S). *Journal of Geophysical Research*, *110*(B1), B01308. https://doi.org/10.1029/2004JB003238

Wimpenny, S. (2022). Weak, seismogenic faults inherited from mesozoic rifts control mountain building in the Andean Foreland. *Geochemistry, Geophysics, Geosystems*, *23*(3), e2021GC010270. https://doi.org/10.1029/2021GC010270

Yáñez, G., & Cembrano, J. (2004). Role of viscous plate coupling in the late Tertiary Andean tectonics. *Journal of Geophysical Research*, *109*(B2). https://doi.org/10.1029/2003JB002494

Yáñez, G. A., Ranero, C. R., Von Huene, R., & Díaz, J. (2001). Magnetic anomaly interpretation across the southern central Andes (32°-34°S): The role of the Juan Fernández Ridge in the Late Tertiary evolution of the margin. *Journal of Geophysical Research*, *106*(B4), 6325–6345. https://doi.org/10.1029/2000JB900337

Zapata, T. R., & Allmendinger, R. W. (1996). Thrust-front zone of the Precordillera, Argentina: A thick-skinned triangle zone. *AAPG Bulletin*, *80*. https://doi.org/10.1306/64ED87E6-1724-11D7-8645000102C1865D

19449194, 2023, 8, Downloaded from https://agupubs.onlinelibrary.wiley.com/doi/10.1029/2023TC007765 by Rwth Aachen Hochschulbibliothe, Wiley Online Library on [15/01/2024]. See the Terms and Conditions (https://onlinelibrary.wiley.com/terms-and-conditions) on Wiley Online Library for rules of use; OA articles are governed by the applicable Creative Commons License